TGF-β blockade drives a transitional effector phenotype in T cells reversing SIV latency and decreasing SIV reservoirs *in vivo*

Jinhee Kim[1], Deepanwita Bose[2]†, Mariluz Araínga[2]†, Muhammad R. Haque[3], Christine M Fennessey[4], Rachel A Caddell[5], Yanique Thomas[3], Douglas E Ferrell[2], Syed Ali[2], Emanuelle Grody[3,9], Yogesh Goyal[3,9,10], Claudia Cicala[6], James Arthos[6], Brandon F Keele[4], Monica Vaccari[5,7], Ramon Lorenzo-Redondo[1,8], Thomas J Hope[3], Francois Villinger[2] and Elena Martinelli[1]

[1]Department of Medicine, Division of Infectious Diseases, Feinberg School of Medicine, Northwestern University, Chicago, IL, USA
[2]New Iberia Research Center, University of Louisiana at Lafayette, New Iberia, LA, USA
[3]Cell and Developmental Biology, Feinberg School of Medicine, Northwestern University, Chicago, IL, USA
[4]AIDS and Cancer Virus Program, Frederick National Laboratory for Cancer Research, Frederick MD
[5]Division of Immunology, Tulane National Primate Research Center, Covington LA, USA
[6]Laboratory of Immunoregulation, National Institute of Allergy and Infectious Diseases, National Institutes of Health, Bethesda, MD, USA
[7]Department of Microbiology and Immunology, Tulane University School of Medicine, New Orleans, LA, USA
[8]Center for Pathogen Genomics and Microbial Evolution, Northwestern University Havey Institute for Global Health, Chicago, IL, USA.
[9]Center for Synthetic Biology, Northwestern University, Chicago, IL, USA
[10]Robert H. Lurie Comprehensive Cancer Center, Feinberg School of Medicine, Northwestern University, Chicago, IL, USA

† Equal contributors
*Corresponding author:

Elena Martinelli

elena.martinelli@northwestern.edu

One-sentence summary:

TGF-β blockade drives an effector phenotype in immune cells leading to SIV latency reversal and enhanced immune responses in vivo.

Abstract

HIV-1 persistence during ART is due to the establishment of long-lived viral reservoirs in resting immune cells. Using an NHP model of barcoded SIVmac239 intravenous infection and therapeutic dosing of the anti-TGFBR1 inhibitor galunisertib (LY2157299), we confirmed the latency reversal properties of *in vivo* TGF-β blockade, decreased viral reservoirs and stimulated immune responses. Eight SIV-infected macaques on ART were treated with four 2-week cycles of galunisertib. ART was discontinued 3 weeks after the last dose, and macaques euthanized 6 weeks after ART-interruption(ATI). All macaques rebounded between week 2 and 6 post-ATI, but one did not. Galunisertib led to viral reactivation as indicated by plasma viral load and immunoPET/CT with ^{64}Cu-DOTA-F(ab')$_2$-p7D3-probe. A decrease in cell-associated (CA-)SIV DNA was detected in lymph nodes, gut and PBMC, while intact pro-virus in PBMC decreased by 3-fold. No systemic increase in inflammatory cytokines was observed. High-dimensions cytometry, bulk, and single-cell RNAseq revealed a shift toward an effector phenotype in T and NK cells characterized by a progressive downregulation in TCF1.

In summary, we demonstrated that galunisertib, a clinical stage TGF-β inhibitor, reverses SIV latency and decreases SIV reservoirs by driving T cells toward an effector phenotype, enhancing immune responses *in vivo* in absence of toxicity.

Introduction

Interruption of antiretroviral therapy (ART) leads to rapid rebound of viremia in the vast majority of people living with HIV-1 (PLWH) due to the establishment of a persistent HIV-1 reservoir early after infection(*1, 2*). A key mechanism of this persistence is the ability of HIV-1 to enter a state of virological latency characterized by the silencing of viral gene expression and/or lack of viral proteins translation(*3, 4*). This allows the virus to remain invisible to the immune system and latently infected cells to survive and proliferate by homeostatic or antigen-driven proliferation(*5, 6*). Of note, the viral reservoir was initially thought to be stable. However, recent evidence suggests that stochastic HIV reactivation under ART occurs, and selective killing is favored in cells bearing replication competent virus integrated in transcriptionally active sites within the genome(*7-9*). Hence, integration site, but especially the activation status of the infected cells profoundly influences HIV-1 persistence.

Ongoing efforts to achieve a functional cure for HIV-1 are directed towards supplementing ART with immunotherapies targeting the viral reservoir. Such strategies, under the umbrella of “shock and kill”, aim to reactivate the replication competent reservoir and eliminate latently infected cells by viral cytopathic effects or immune-mediated killing (*10, 11*). However, these strategies have thus far failed to achieve a reduction of the viral reservoir or post-ART virologic control in either the clinic or preclinical models. This is mainly due to the low inducibility of latent proviruses and the heterogeneity of the mechanisms of persistence(*12, 13*) (*14, 15*). In contrast, therapeutic vaccination strategies focused on enhancing HIV/SIV-specific responses have had some discreet measure of success(*16*). However, currently, no single strategy leads simultaneously to latency reversal and stimulation of effective immune responses.

The HIV life cycle and HIV’s ability to replicate efficiently are especially dependent on the activation status of the infected cells. In this context, significant advances have been made to directly activate immune cells through non-canonical pathways in order to promote HIV latency reversal(*17*). However, the activation and differentiation of immune cells is intrinsically linked to

80 cellular metabolism(*18*). Indeed, signaling pathways that govern immune cell differentiation and
81 activation such as mTOR and Wnt/β-catenin, not only have been implicated in regulating HIV
82 latency(*19-21*), but are also critical regulators of cell metabolism(*22*). The metabolic status of an
83 infected cell, in turn, plays a critical role in its ability to support latency reactivation and viral
84 production(*19, 23*).
85 In this context, recent evidence suggests that TGF-β plays a critical role in the regulation of
86 immune cell activation and metabolic reprogramming(*24-26*). Specifically, in the context of $CD8^+$
87 T cells, TGF-β has been shown to suppress mTOR signaling preserving the metabolic fitness of
88 memory $CD8^+$ T cells(*25*) and stem-like antigen specific $CD8^+$ T cells through its modulation of
89 Wnt/β-catenin factor TCF1(*26, 27*). TCF1 and the mTOR pathway are also critical to T cell
90 differentiation and responsible for the transition from activated effector cells to resting memory
91 cells during LCMV infection(*22, 26*). The regulation of quiescence in $CD8^+$ T cells that follows
92 continuous TGF-β stimulation is critical to the transition to a memory phenotype and it is driven
93 by specific metabolic changes that are linked to decreased glycolytic activity, more efficient
94 mitochondrial respiration, and long-term survival(*25, 26*).
95 Similarly, in the context of NK cells, TGF-β has been implicated in decreasing their baseline
96 metabolism driving lower expression of markers of NK cytotoxic activity(*28*).
97 While TGF-β-mediated suppression of TCR and IL-2 signaling were shown to lead to lower $CD4^+$
98 T cell activation following cognate antigen recognition in older studies(*24, 29*), more recent work
99 using $CD4^+$ T cell-specific deletion of the TGF-β receptor demonstrated an even more profound
100 effect of TGF-β on all stages of $CD4^+$ T cell activation, proliferation and cytotoxic response to
101 LCMV than in $CD8^+$ T cells(*30*). However, little is known on the specific role of TGF-β in regulating
102 the transition to and from memory and effector phenotypes in $CD4^+$ T cells and how this may be
103 associated with TGF-β-driven changes in $CD4^+$ T cells metabolism. Moreover, TGF-β regulates
104 the expression of CD103 and other surface and intracellular factors essential of T cell residency

105 in mucosal tissues(*31-33*). Hence, TGF-β is considered the master regulator of mucosal
106 immunity(*34*).
107 We and others have recently demonstrated that TGF-β regulates HIV-1 latency in primary $CD4^+$
108 T cells ex vivo and in vivo(*35-37*). Latency reversal was detected in a non-human primate (NHP)
109 model of HIV infection following a short treatment with a clinical stage TGF-β inhibitor, galunisertib
110 (LY2157299)(*38*). In that previous study, we documented latency reversal particularly at the level
111 of the gut mucosal tissue using the ^{64}Cu-anti-gp120 Fab_2(7D3) probe and immuno-PET/CT(*35*).
112 In that study, we further validated the ability of immune-PET/CT to identify sites of viral reactivation
113 and replication in the gut by performing tissue resection in hot areas of the gut identified by PET
114 followed by confirmatory PCR for vDNA/RNA and vRNAscope(*35*).
115 Herein, we demonstrate how treatment with galunisertib with a 2-week on, 2-week off regiment
116 that mimics the therapeutic regimen employed in the clinic in phase 1 and 2 trials of solid
117 tumors(*39, 40*), leads to profound transcriptional and functional changes in immune cells in the
118 absence of overt toxicity or increased systemic inflammation. Importantly, we observed a shift
119 toward a transitional effector phenotype in $CD4^+$ T cells and other immune cells both systemically
120 and in the lymph nodes. This shift was accompanied by, and likely responsible for, increased viral
121 reactivation in SIV-infected, ART treated macaques documented by molecular techniques and
122 PET/CT images. At the end of the treatment with galunisertib, we detected lower viral reservoir
123 levels, including total and intact proviral DNA in both PBMC, gut and lymph nodes and significantly
124 higher immune responses.
125
126 **RESULTS**
127 **2-weeks on-off therapeutic regiment with Galunisertib leads to viral reactivation SIV**
128 **infected, ART-treated macaques.**
129 To confirm galunisertib-driven HIV/SIV latency reversal and investigate the underlying
130 mechanisms, 8 Indian origin rhesus macaques (*Macaca Mulatta*, Mamu-A01-, -B08, -B17-, all

131 females) were infected intravenously with 300 TCID50 of the barcoded SIVmac239M2. We
132 initiated ART treatment (daily co-formulated Tenofovir [PMPA], Emtricitabine [FTC] and
133 Dolutegravir [DTG]) on week 6 post-infection (pi). A 2-week on, 2-week off therapeutic cycle with
134 galunisertib (20mg/Kg twice/daily orally) started at week ~35pi and continued for a total of 4 cycles
135 (Fig 1A and Table S1). ART was discontinued 3 weeks after the last galunisertib dose, and the
136 macaques were followed for 6 weeks after ART discontinuation. Median peak plasma viral load
137 (pVL) was 10^8 copies/ml at week 2pi. A rhesus anti-PD1 antibody was administered at 5mg/kg
138 before the 3rd and 4th cycle to 2 macaques (08M156 and A6X003). However, no differences were
139 noted for these 2 macaques in any of the parameters we measured, and the data were pooled.
140 Full suppression to undetectable levels (pVL LOD 15 copies/ml) was achieved in 3 out of the 8
141 macaques at week 10pi. In the other 5 macaques, pVL fell below 65 copies/ml by week 22pi with
142 a single blip of 400 copies/ml in A8T010 at week 29pi (Fig 1B). Following the start of the
143 galunisertib treatment, pVLs increased in 7 out of 8 macaques from a single peak over
144 undetectable in 08M171 and A8L057 to several peaks and up to 10^3 copies/ml in the other
145 macaques. Of note pVLs in A8T010 and A8R095 was undetectable for over 5 weeks before,
146 respectively, blips of up to 10^2 copies/ml were detected following galunisertib treatment initiation
147 (Fig 1B). More frequent blips were noted during the first 2 cycles with galunisertib compared to
148 cycles 3 and 4 (Fig 1C). However, 08M171 and A8L057 did not experience a pVL increase until
149 the 4th cycle.
150 Importantly, we documented viral reactivation also using immunoPET/CT. The ^{64}Cu-anti-gp120
151 Fab_2(7D3) probe was injected 24hrs before and after, respectively, the beginning and the end of
152 the first 3 galunisertib cycles and scans performed before and after the first and the last dose
153 24hrs after probe injection. As shown in Fig 2, Fig S1 and Movies S1-S8, the PET signal visibly
154 increased in different tissue areas after cycle 2 (in A8R095, 08M156, A8L014 and A8T010) or at
155 the beginning of cycle 3 (in A6X003, 08M134 and A8L057). In 08M171 we observed an increase
156 in the gut area only at the beginning of cycle 2 and an issue with probe stability in cycle 3 led to

157 exclusion of the last 2 scans of 08M171 from the analysis. Hence, the last 2 time points of 08M171
158 were excluded from the analysis (Fig S1, 08M171 infection, treatment and scan were offset
159 compared to the other macaques). A corresponding increase in mean standard uptake values
160 (SUV) was detected in the gastrointestinal area and axillary lymph nodes (Fig 2B) and was
161 significant in cycle 3 compared to before cycle 1 (BC1). In these anatomical areas (ROIs in Fig
162 S2 and Movies 9-10), SUV increases correspond to increases in viral replication as shown in
163 previous studies(*41, 42*). A PET signal increase was also noted in the area of the vertebral column
164 (spine) and nasal associated lymphoid tissues (NALT). However, neither cerebrospinal fluid (CSF)
165 nor bone marrow (BM) or NALT tissue were collected during the study, and we have no prior
166 validation of the specificity of the signal in these anatomical locations. Hence, whether this signal
167 corresponds to increased viral replication and whether this occurs in the vertebral bones or
168 cerebrospinal fluids remains to be determined. No SUV increase was present at the level of the
169 spleen or kidney, where probe accumulation and background signal likely masked any specific
170 signal. However, a significant increase in SUV was detected in the liver (Fig 2B). Similar increases
171 in PET signal are evident also when considering the normalized Total Lesion Glycolysis
172 (SUVbw*ml) values (a value generally independent of the matrix used for analysis; Fig S3A) in
173 these anatomical areas. Blood pool activity (BPA) also increases during the 3rd cycle (Fig S3B).
174 Whether this is due to galunisertib-specific effects or changes in virus remains to be determined.
175 However, when the mean SUV was normalized for BPA in the gut, axillary lymph nodes and spine,
176 the signal increase in the 3rd cycle was lost, but an increase during the first cycle became evident
177 (Fig S3C). Of note, the non-BPA normalized SUVmean increase in the gut and lymph node areas
178 in most cases followed an increase in cell-associated vRNA detected, respectively, in colorectal
179 biopsies and fine needle aspirates (FNA) at the same time points during treatment (Fig S4).
180
181 **A 4 cycle treatment with galunisertib decreases viral reservoir in absence of systemic**
182 **inflammation.**

183 To determine the impact of galunsiertib on SIV reservoir, we measured CA-vDNA in PBMC,
184 colorectal biopsies and lymph nodes (LN). A significant decrease in CA-vDNA was detected in all
185 tissues between week 35pi (beginning of cycle 1, BC1) and week 49pi (after/end of cycle 4, AC4)
186 for gut and LN, and between week 35pi (BC1) and end of cycle 3 (AC3) for PBMC (Fig 3A, AC4
187 not measured for PBMC and Fig S5A). In the gut and LN (right axillary), decreases ranged from
188 a Log to 1/3 of a Log (gut: median 0.77; range:0.33-0.94 folds LN: median: 0.93; range:0.33-0.98
189 folds decrease). In the PBMC the decrease was slightly less pronounced with a median half Log
190 decrease (median: 0.58; range 0.28-0.88 folds decrease). However, the comparison for the
191 PBMCs was between week ~35 and week ~45 (end of cycle 3, AC3) instead of the end of all 4
192 cycles, because a snap frozen pellet was not available at the end of cycle 4 for PBMCs. The SIV
193 reservoir in PBMCs was also monitored by SIV-IPDA comparing before cycle 1 (BC1) to the end
194 of cycle 4 (AC4). Of note, we observed significant decreases of both total and intact provirus by
195 SIV-IPDA. Intact provirus declined similarly to the CA-vDNA with a median of half Log (median:
196 0.53; range:0-0.71 folds decrease).
197 In contrast, no decline in CA-vDNA was detected in the PBMCs of a group of 4 macaques infected
198 intravenously with the same stock of SIVmac239M2 for a separate study. These 4 macaques
199 were placed on ART on week 6pi as in our study. However, no decline in CA-vDNA was detected
200 under ART, between weeks 28 and 52pi (untreated group, Fig S5B). Thus, we conclude that the
201 decline in CA-vDNA in PBMC was not due to ART-alone.
202 Importantly, we found no significant changes in any of the clinical variables (chemistry and
203 hematology, Tables S2 and S3) measured before, during and after the galunisertib therapy.
204 Moreover, we observed no changes in the concentrations of inflammatory chemokines and
205 cytokines measured in plasma before and after the first 2 treatment cycles and at the end of the
206 last cycle (Fig 3C). The only difference in cytokine and chemokine levels after galunisertib
207 treatment was a small increase in IL-10 detected at the end of the last cycle compared to before
208 treatment (Fig S5C).

209

210 **Galunisertib treatment drives an effector phenotype in T and NK cells.**

211 The phenotype of PBMCs before and after Galunisertib treatment was monitored by high-
212 parameter flow cytometry of T and NK cell subsets and phenotype (Table S4). Classical subsets
213 and single-color analysis of MFI revealed a substantial increase in the expression of CD95 and a
214 profound consistent decrease in TCF1 expression in $CD4^+$ T cells that continued throughout the
215 treatment (Fig 4A). In contrast, a small decrease in CD62L after the first cycle, reverted to baseline
216 during the following cycles. The frequency of naïve cells, defined as $CD95^-$ within $CD4^+$ T cells,
217 decreased in parallel with the increase in CD95 (gating strategy in Fig S6). Interestingly, there
218 was no change in the expression of CCR7 or CD28 within $CD95^+$ $CD4^+$ T cells (Fig 4B). Hence,
219 the frequency of central memory and effector memory as defined by CD95 and CD28 or CCR7
220 did not change (Table S5). The levels of T-bet did not change significantly (Fig S7A). However,
221 we detected a downregulation of the gut homing receptor integrin $\alpha4\beta7$ and a decrease in the
222 levels of granzyme B (GRZB, Fig S7A). Of note, the expression of activation markers CD69, HLA-
223 DR and Ki67 remained mostly unchanged, with the exception of an increase in HLA-DR at the
224 beginning of cycle 2 compared to before galunisertib (Fig 4C). Interestingly, the effect of
225 Galunisertib on $CD8^+$ T cells was not as pronounced as it was on $CD4^+$ T cells. No significant
226 increase was detected in CD95 expression and TCF1 downregulation reached significance only
227 at the end of the treatment (Fig 4D). Markers of cell activation like HLA-DR, Ki67 and CD69 did
228 not change (Fig 4D and Fig S7B). However, we detected a significant decrease in T-Bet at the
229 beginning of cycle 2 (BC2) compared to before treatment (BC1). Finally, in contrast to $CD4^+$ T
230 cells, the decrease in GRZB was more pronounced at several time points during treatment and
231 there was a sustained significant increase in CCR7 expression in memory $CD8^+$ T cells (Fig 4E).
232 Interestingly, the expression of PD1 on both $CD4^+$ T cells and $CD8^+$ T cells either did not change
233 or was slightly downregulated. Importantly, the frequency of $PD1^+$ $CD101^+$ ($TCF1^{low}$) exhausted
234 memory $CD8^+$ T cells(*43*) did not change (Fig S7B). Finally, within $NKG2A^+$ $CD8^+$ NK cells, there

235 was a pronounced increase in CD16 expression and an initial increase in the proliferation marker
236 Ki67 (AC1 vs BC1; Fig 4F).
237 High-dimensional data visualization with tSNE and clustering analysis with FlowSOM(*44*)
238 confirmed the results of the classical analysis. We performed tSNE and FlowSOM after data clean
239 up with FlowClean and normalization with the SwiftReg algorithm(*45*). The analysis was
240 performed on before (BC1) and after the last cycle (AC4) only (Fig 4G and Fig S8A) and on all
241 time points analyzed (Fig S8B and S8C). When we compared only BC1 and AC4, the
242 PhenoGraph clustering algorithm identified 36 populations. FlowSOM with 36 populations
243 identified 6 populations of $CD4^+$ T cells, 6 of $CD8^+$ T cells and 4 of NK cells ($NKG2A^{high}$ $CD8^+$; Fig
244 S8A). The remaining populations were likely monocytes and other minor subsets. Direct
245 comparison of each population revealed a decrease in Pop 31 (naïve CD8 T cells) and Pop 30
246 (central memory $Ki67^+$ $CD8^+$ T cells) and an increase in Pop 2 and 3 (effector and central memory
247 $CD4^+$ T cells). Finally, there was a decrease in HLA-DR high Pop0 and an increase in $CD16^{high}$
248 $NKG2A^-$ Pop14 (Fig 4H and S8A). Visual inspection of the tSNE plots (Fig 4G) revealed 3 areas
249 mostly occupied by cells in the post-galunisertib AC4 group (New1, 2 and 3) which were
250 characterized by high levels of CD16 and GRZB (New 3 is likely NK cells). In contrast, 3 areas
251 mostly occupied by cells in the pre-galunisertib group BC1 (Old1, 2 and 3) were characterized by
252 high levels of TCF1 and low CD95, confirming the finding of the classical analysis. Analysis of all
253 time points with phenograph-derived 38 populations in FlowSOM recapitulated findings obtained
254 with the classical analysis and the BC1 AC4 comparison with no additional insights (Fig 4I).
255
256 **Galunisertib treatment in vivo increases pTreg while decreasing pTfh**
257 The frequencies of circulating Tregs and Tfh cells were monitored with an established flow
258 cytometry panel(*46, 47*) after the first and third cycle of galunisertib. The frequency of all $CD4^+$
259 Tregs ($CD25^{high}$ $FoxP3^+$; gating in Fig S9) and $CD8^+$ Tregs increased after the first cycle and
260 remained higher until the end of the 3rd cycle, while $CCR4^+$ Treg were proportionally higher at the

261 end of the treatment compared to before (Fig 4J). In contrast, circulating Tfh ($CXCR5^+$ $PD1^+$;
262 gating in Fig S9) were lower at the end of the Galunisertib treatment both within total and central
263 memory $CD4^+$ T cells (Fig 4J). Finally, the expression of CD39 (ecto-nucleotide triphosphate
264 diphosphohydrolase 1), which tracks within extracellular adenosine and immunosuppressive
265 effects, was lower on total and central memory $CD4^+$ T cells (Table S5 and Fig 4J, respectively).

266

267 **Bulk RNAseq of PBMC and single-cell (sc)RNAseq analysis of LN confirm a profound shift**
268 **toward effector phenotype.**

269 In our previous studies, we determined that 6hrs after galunisertib treatment in naïve macaques
270 there was an upregulation of the AP1 complex (JUN and FOS) and several genes encoding
271 ribosomal proteins in $CD4^+$ T cells(*42*). To understand early and later effect of galunisertib in the
272 context of SIV infection, in the current study we performed bulk RNAseq of PBMC isolated 1hr
273 after the first administration of galunisertib in cycle 1 and at the end of the 1st 2-weeks cycle. We
274 found 640 genes significantly modulated (FDR<0.05; abs(log_2 FC(Fold Change))>2) in PBMC just
275 1hr after the first dose of galunisertib. The majority (457 genes) were downregulated (Fig 5A).
276 Gene set enrichment analysis (GSEA) revealed an upregulation of the oxidative phosphorylation
277 (OXPHOS; Enrichment Scores (ES) 0.58 FDR=0.048) and the reactive oxygen (ES 0.55
278 FDR=0.075) pathways among the Hallmark genet sets (Fig 5A and S10). Among the Biocarta
279 sets, there was an enrichment in the electron transport chain (ETC; ES 0.84 FDR=0.132) and a
280 downregulation of the circadian (ES -0.81 FDR=0.163) pathways (Fig 5A and S10). Finally, among
281 the top modulated genes (by FC) there were several genes encoding for soluble transporters,
282 while classical activation markers like CD69 and CD38 were downregulated (Fig S10B). An early
283 engagement of metabolic pathways was confirmed by enrichment analysis of significant DEG with
284 Metascape(*48*) with an upregulation of adipogenesis, OXPHOS and fatty acid metabolism (Fig
285 S10C). Of note, 2 weeks after the beginning of galunisertib, metabolic pathways were still among

286 the most enriched upregulated pathways in PBMCs (Fig 5B and Fig S11A). Among the top
287 upregulated genes there were CD44, CCR5, several integrins and GRZA and GRZB (Fig S11B).
288 Finally, we performed bulk RNAseq of rectal biopsy tissue before and after the first cycle with
289 galunisertib (Fig 5C). There were only 51 differentially expressed genes (DEGs; FDR<0.05;
290 $log_2FC=2$). GSEA analysis of all DEGs (FDR<0.05) revealed the G2_M_DNA replication pathway
291 highly enriched (ES 0.97 FDR=0.012) within the Hallmark set. Among the most interesting
292 changes, we observed a pronounced downregulation of integrin β7, in contrast to an increase in
293 integrin αE (CD103; Fig 6C), suggesting that TGF-β-driven increase in αE(*49*) may be driven by
294 non-canonical TGF-β pathway signaling not blocked by galunisertib.
295 To clarify the impact of galunisertib at the single cell level and in lymphoid tissues, we also
296 performed scRNAseq analysis of cells isolated from LNs before (right axillar) and after (right or
297 left inguinal) the first cycle (Fig 6). Dimensionality reduction and clustering analysis with PCA and
298 uniform manifold approximation and projection (UMAP)(*50*) was performed to visualize the data
299 (Fig 6A). However, cells were classified based only on gene expression (Fig 6B and C). We first
300 classified major subsets: T cells (38,705 cells), B cells (31,385 cells), NK cells (1,628 cells),
301 macrophages (285) and cells expressing both CD19 and CD3 (942 T/B cells) (Fig 6A shows this
302 classification over UMAP). Then we classified only $CD4^+$ and $CD8^+$ T cell subsets (Fig 6C and
303 S12A) and B/T subsets including naïve and germinal center (GC) B cells and Tfh cells (Fig S12B
304 and S12C). Cell number for all these subsets did not change with treatment (Fig S13). However,
305 differential gene expression analysis of T cells revealed an upregulation of members of the AP1
306 complex, CD69, β2 macroglobulin and RPL13 among the most upregulated genes (Fig 6D).
307 Moreover, it confirmed a downregulation of TCF1 at the transcriptional level (TCF7 gene; Fig 6D).
308 Gene enrichment analysis revealed again Myc_targets_V1, OXPHOS and mTORC1 as the most
309 enriched hallmark pathways (Fig 6E). Of note, among gene ontology cellular processes, RNA
310 processing was the most highly enriched pathway with intracellular transport and catabolic

311 processes following right after (Fig S14A) confirming an increase in translation and metabolism
312 within these cells.
313 Since we noticed substantial differences in the impact of galunisertib on $CD4^+$ T cells compared
314 to $CD8^+$ T cells by flow, we focused the analysis on these subsets. In $CD4^+$ T cells we found only
315 25 DEGs with a $log_2FC=0.15$, while 34 DEGs were in $CD8^+$ T cells with more downregulated
316 genes in the $CD8^+$ T cells compared to the $CD4^+$ T cells. The AP1 complex and TCF7 were again
317 upregulated and downregulated respectively in both $CD4^+$ (Fig 6F) and $CD8^+$ T cells (Fig 6G).
318 However, STAT1 was more strongly downregulated in $CD4^+$ T cells. Enrichment analysis showed
319 once again upregulation of Myc_targets_V1, OXPHOS and mTORC1 pathways in both $CD4^+$ and
320 $CD8^+$ T cells (Fig 6H and Fig S14B). Interestingly, the most enriched set among in Biocarta was
321 the HIV-Nef pathway (Fig 6J) demonstrating the relevance of these galunisertib-driven changes
322 to HIV cell cycle and transcription (highly enriched KREB pathway as well). The 2nd most enriched
323 Biocarta pathway was TCR signaling, linking galunisertib to cell activation. Next, we analyzed
324 changes in gene expression in Tfh cells. In this subset we obtained a similar number of DEG as
325 in other T cells and myc_targets_V1 was still the most enriched hallmark pathway (Fig S14C and
326 D). In B cells, the AP1 complex was again prominently upregulated, together with CD83, CD69
327 and MAMU-DR. Of note, more genes were modulated in B cells (44 genes with a $log_2FC=0.15$
328 and 18 with logFC0.2) than in T cells with some differences in enriched pathways (Fig S14F).
329 Similar genes were modulated in GC B cells and naïve B cells with several more DEGs in naïve
330 B cells than in GC cells (Fig S15A and B). Finally, 144 genes were modulated in NK cells and 39
331 genes in macrophages (Fig S15C and D; $log_2FC=0.15$). GRZB was prominently upregulated, but
332 CD44 downregulated. In macrophages genes were mostly downregulated including TCF7L2 and
333 KLF4 suggesting an increase in inflammatory phenotype and decrease in M2 polarization(*51*) (Fig
334 S15D).
335
336 **Galunisertib increases SIV-specific responses and changes barcode distribution**

337 In order to understand how galunisertib affected immune cell function and SIV-specific responses,
338 we stimulated PBMC with 15-mer SIV peptides from SIVmac239 gag, pol and env for 24hrs on
339 antibody coated Elispot plates. Because of sample availability, we probed before and after the
340 first cycle and after the 3rd galunisertib cycle only. Interestingly, by the end of the 3rd cycle there
341 was a significant increase in IFN-γ secretion both SIV-specific (particularly against env) and non-
342 specific (DMSO control). TNF-α release increased particularly in response to Gag and non-
343 specifically (Fig 7). However, IL-2 release appeared to increase slightly after the first cycle (non-
344 significant), but remained unchanged with a slight decrease by the end of the 3rd cycle (Fig 7).
345 In order to understand if these changes in immune responses in combination with latency reversal
346 and switch toward an effector phenotype may have impacted viral population dynamics, we
347 analyzed changes in numbers and distribution of the viral barcodes before and after the first 3
348 treatment cycles. There was no barcode amplification at several time points particularly in the
349 lymph nodes. However, although there were no significant changes in the number or diversity
350 (measured as Shannon Entropy; Sh) of barcodes before and after each galunisertib cycle (Fig
351 S16A and Fig 8A), we found significant changes in barcode frequency distribution in most tissues
352 and cycles after galunisertib treatment (Fig 8B and S16B). Specifically, the relative proportion of
353 each barcode changed in all monkeys in all cycles in the rectal biopsies (probably a consequence
354 of different sampling area), but also for all LN analyzed (except for 08M134 in cycle 1). Of note,
355 the same LN were sampled at the beginning and after cycle 3 (Table S6). Hence, sampling
356 location does not explain the changes barcode distribution. Changes in the proportion of barcodes
357 were also detected in at least half of the PBMCs after cycle 1 and 2 (cycle 3 not analyzed). Finally,
358 barcode diversity decreased in plasma post-ATI compared to the time point right before ART (Fig
359 8C) and barcode distribution significantly changed post-ATI compared to pre-ART in 2 of the 7
360 macaques that rebounded (Fig S16C).
361

362 **TCF1 downregulation in CD4$^+$ T cells correlates with virological and immunological**
363 **endpoints.**
364 In order to explore a possible association between the various virological and immunological
365 parameters and their changes, we built a correlation matrix with a curated set of variables of
366 interest or their fold changes. This analysis revealed an association between the decrease in
367 TCF1 expression in the CD4$^+$ T cells and several virological and immunological variables (Fig
368 8E). Specifically, both the levels of CA-vDNA in the colorectal tissue and the fold increase in gut-
369 SUV strongly inversely correlated with fold changes in TCF1. Since TCF1 decreased, a larger
370 decrease in TCF1 was directly proportional to residual vDNA in the gut at the end of cycle 4 and
371 to the increase in PET signal in the gut (Fig 8D and 8E). A weaker, but still significant association
372 was also present with CA-vDNA in PBMC at the end of cycle 3 and with the levels of vRNA in the
373 lymph nodes at the end of the 4th cycle (Fig 8D and S17A). Finally, the decrease in TCF1
374 correlated with the increase in IFN-γ and poly-functional IFN-γ/TNF-α releasing cells (cumulative
375 increase of SIV-specific responses to gag, pol and env; Fig 8D and 8E). Of note, the increase in
376 PET signal in the gut also correlated with the levels of vDNA in PBMC at the end of cycle 3, vDNA
377 in gut biopsies and residual CA-vRNA in LN at the end of cycle 4 (Fig S17B). Interestingly, the
378 levels of residual CA-vRNA in LN also correlated with the increase in IFN-γ and poly-functional
379 IFN-γ/TNF-α releasing cells (Pearson r=0.85 and 0.76, respectively). Finally, the residual intact
380 pro-virus (IPDA) directly correlated with the levels of IFN-γ and IFN-γ/TNF-α produced in response
381 to SIV peptides at the end of cycle 3 (Fig 8D; r= 0.76 and 0.88, respectively). In contrast, the
382 change in intact provirus trented to correlate inversely with the levels of IFN-γ, so that a larger
383 decrease directly correlated with more IFN–γ responses. However, this did not reach significance
384 (p=0.117, Fig S17C).
385
386 **Discussion**

387 HIV-1 latency in T cells is maintained through diverse mechanisms that include blocks in
388 transcriptional elongation, completion, and splicing(*13*). A common characteristic shared by HIV-
389 1 latently infected cells of both T and myeloid cell lineages is their "resting" phenotype(*14, 52-54*)
390 In these cells, an inability to transcribe proviral DNA is linked to a generalized decrease in
391 transcriptional activity which, in turn, is linked to their metabolic status(*23*). Cellular metabolism is
392 in turn influenced by tissue location and environmental cues(*55*).
393 TGF-β is released at high level in PLWH and its levels remain high during ART(*56*). The
394 immunosuppressive activity of TGF-β is well-known. However, the effect of TGF-β signaling in
395 immune cells is highly context dependent(*57*). Hence, TGF-β plays different roles according to a
396 cell differentiation and activation status(*57*). In $CD8^+$ T cells and NK cells, TGF-β was shown to
397 decrease mTOR activity and preserve cellular metabolism (high mitochondrial activity and spare
398 respiratory capacity, but reduced mTOR activity) preventing metabolic exhaustion(*25, 26, 58, 59*).
399 This effect was linked to survival of antigen-specific $CD8^+$ T cells, preservation of their stemness
400 and it was linked to higher expression of the TCF1 factor(*25*).
401 In contrast, in $CD4^+$ T cells TGF-β is known to decrease TCR activation(*29, 60*), restrict
402 proliferation and inhibit cytotoxicity (including granzyme and perforin release) at different stage of
403 infection in vivo(*30, 61*). However, the role of TGF-β in the formation and preservation of $CD4^+$ T
404 cell memory is still unclear(*57*). Moreover, the link between TGF-β signaling and TCF1 expression
405 in $CD4^+$ T cells is unexplored.
406 Here, we used a clinical stage small drug, galunisertib, developed by Eli Lilly and used in several
407 phase 1 and 1/2 clinical studies against solid cancer(*39, 62, 63*) to investigate the impact of TGF-
408 β blockade on SIV latency, SIV reservoir and immune responses. Of note, Eli Lilly did not
409 terminate galunisertib development program because of toxicity(*64, 65*). Indeed, in our studies in
410 macaques, we observed no adverse events nor changes in chemical or hematological variables.
411 Moreover, there were no detectable changes in the levels of the 24 inflammatory factors that we

412 probed in plasma during the treatment. This suggests that this therapeutic approach may be safe
413 in people living with HIV (PLWH).
414 The first important finding of our study was the confirmation of our previous report of the latency
415 reversal properties of TGF-β blockade in vivo(*35*). Indeed, we found increase in pVL in 7 out of
416 the 8 macaques upon initiation of galunisertib therapy. Although not all macaques were fully
417 suppressed before treatment, substantial increases in pVL (>10^2 copies/ml) were noted also in
418 fully suppressed macaques (08M171, A8R095 and A8L057). Moreover, viral reactivation was
419 documented in tissues by immunoPET/CT. The increase detected post-galunisertib in gut SUV
420 correlated with CA-vRNA as in our previous studies(*35*) and, interestingly, it was associated with
421 a decrease in TCF1. Galunisertib led to increased probe uptake in the gut and lymphoid tissues.
422 Yet, there was no change in the PET background signal in kidneys and spleen. This increase was
423 still present during the 1st, but not the 3rd cycle when normalizing SUVmean over BPA. Since our
424 probe is a Fab2 and not a full antibody, we did not expect the probe to be still present in significant
425 amounts in blood in a scan performed 24hrs post-infection. Nonetheless, we detected significant
426 changes in BPA that may be due to galunisertib or the interaction of galunisertib with increases
427 viral antigen. TGF-β is required for vascular barrier function(*66*). Hence, galunisertib may have
428 increased vascular permeability. However, this would lead to a decrease BPA instead than an
429 increase and significant changes in VEGF-A were not noted. This, in conjunction with our previous
430 studies validating the specificity of the PET signal for areas of enhanced SIV replication in gut
431 and lymph nodes(*35, 41, 67*), demonstrates that the galunisertib-driven increases in SUV were
432 mostly specific, and highlighted areas of SIV latency reversal at least in gut and lymphoid tissues.
433 The extent to which the increased signal in the spine and bones recapitulates an increase in SIV
434 replication at these sites remains to be determined.
435 Importantly, we observed a decrease in CA-vDNA in all the tissues that cannot be attributed to
436 ART alone. Indeed, although we did not have a concurrent control group, this decrease was not
437 present in similar studies conducted in SIVmac239M2 infected macaques on the same ART

438 regimen, but not treated with galunisertib. Considering studies by other groups with different
439 models (SIVmac251), they report 2nd phase decay of SIV intact provirus (weeks ~32 to ~100pi,
440 Fig 2B in(*68*)) with a $t_{1/2}$ of >8 months(*68*). In contrast, in our study, the intact provirus decreased
441 by 3 folds (median) in a little over 3 months (from week 35pi, BC1 to week 49pi, AC4). Interestingly,
442 this decrease in intact pro-virus trended toward a direct correlation with IFN-γ responses.
443 However, IFN–γ levels also inversely correlated with the absolute value of residual intact provirus,
444 suggesting that IFN-γ responses were driven by residual viral reservoir while, at the same time,
445 were involved in clearing intact virus. Indeed, the increase in IFN-γ and TNF-α also correlated
446 with residual CA-vRNA in the LN at the end of the treatment. The latter, in turn, was directly
447 proportional to the increase in gut SUV. This is in line with increased latency reversal explaining
448 residual viral RNA in lymphoid tissues.
449 Finally, one of our most intriguing results was the profound downregulation of TCF1 in CD4$^+$ T
450 cells at both the transcriptional and protein levels. Although TCF1 is conventionally viewed as an
451 effector of the canonical Wnt pathway(*69*) and recently reached notoriety for its role in maintaining
452 stemness of antigen-specific memory CD8$^+$ T cells(*26, 70*), TCF1 has a plethora of functions in T
453 cell development and differentiation largely independent of Wnt signaling(*22*). In CD4$^+$ T cells,
454 TCF1 has been implicated in orchestrating all the major Th subsets, including Th1, Th2, Th17
455 and Tfh(*71*). TCF1 is known to control the bifurcation between Th1 and Tfh in favor of Tfh
456 cells(*71*), while it negatively regulates Treg development(*22*). This is in line with our findings of
457 increased Treg and decreased Tfh, in the midst of a profound downregulation of TCF1.
458 Importantly, TCF1 is downregulated with increased cellular differentiation and progression toward
459 effector functions in T cells. T cell activation leads to reduced levels of TCF1 and higher levels of
460 TCF1 are present in T cells with higher stemness and low anabolic metabolism(*69*). These
461 findings suggest that TCF1 has a critical role in maintaining quiescence in immune cells likely in
462 concert with TGF-β(*18, 61*). Our data reveal that this link may be even more prominent and

463 important in $CD4^+$ T cells than in $CD8^+$ T cells. Importantly, the decrease in TCF1 was
464 accompanied with enhancement in other effector markers such as CD95, CD16 and GRZB (at
465 the transcriptional level) and an increase in the transcription of AP1 complex. However, there was
466 no clear upregulation of other classical markers of immune activation such as CD69 and no
467 increase in T cell proliferation (Ki67 expression). Hence, galunisertib treatment does not appear
468 to lead to classical T cell activation. Instead, in vivo TGF-β blockade seems to primarily change
469 the metabolic state of T cells (and likely other immune cells) increasing OXPHOS and
470 mitochondrial function. Of note, although glycolysis is essential during cell activation,
471 mitochondrial pathways are engaged and remodeled early after activation and OXPHOS
472 upregulation has a pivotal role in the earliest stages of cell activation(*18*).
473 Hence, we propose a model in which TGF-β inhibition forces cells (particularly $CD4^+$ T cells) out
474 of quiescence to a transitional state where they reinitiate their transcriptional program and are
475 metabolically ready to be activated and effector. In absence of direct TCR engagement or other
476 activation stimuli, they do not undergo full/classical activation and proliferation, yet they can
477 reinitiate viral transcription and respond to SIV antigenic stimulation. Indeed, functionally, we
478 demonstrated that the PBMC after galunisertib treatment secrete higher levels of IFN-γ and TNF-
479 α. Interestingly, there was no increase in IL-2 secretion. The link between TGF-β and IL-2(*72*)
480 and the critical role of IL-2 in T cell proliferation again suggest that galunisertib enhances an
481 effector phenotype uncoupled from cellular proliferation. scRNAseq analysis demonstrated a
482 trend toward an effector phenotype also in other immune cells, such as B cells, NKs and
483 macrophages. Future studies will need to uncover in depth the effect of TGF-β blockade on these
484 other immune subsets.
485 This study has several limitations. The most important limitations are the relatively small number
486 of macaques and the lack of a concurrent untreated control group. We also could not investigate
487 in depth the viral kinetics after ART interruption because of the short follow up after ATI. Moreover,

488 we did not explore changes in the phenotype or turnover of cells isolated from gut and lymph
489 nodes and relied solely on transcriptional data for these tissues. Finally, because of sample
490 availability, we could not dissect the cellular origin of increased IFN-γ and TNF-α.
491 In conclusion, we report that in vivo treatment with a clinical stage small molecule TGF-β inhibitor
492 drives an effector phenotype in T cells that is likely responsible for increasing the frequency of
493 spontaneous latency reversal events, stimulating SIV-specific immune responses, and
494 decreasing the viral reservoir. Future work will determine whether the galunisertib-driven
495 enhanced antiviral responses and decreased viral reservoirs can significantly contribute to post-
496 ART virological control.
497

498 **MATERIALS AND METHODS**

499 **Study design and Ethics Statement**

500 A total of 8 adult female Indian origin *Rhesus* macaques (*Macaca mulatta*; Mamu A*01, B*08 and
501 B*17 negative) were used for the study described in the manuscript (Table S1). All the macaques
502 were selected form the colonies bred and raised at the New Iberia Research Center (NIRC),
503 University of Louisiana at Lafayette. Treatments were in accordance with NIRC standards which
504 comply with the Guide for the Use and Care of Laboratory Animals. Any abnormal observations
505 and/or signs of illness or distress were reported per NIRC SOPs. Appropriate procedures were
506 performed to ensure that potential distress, pain, discomfort were limited to that unavoidable in
507 the conduct of the research plan. Ketamine (10mg/kg) and/or telazol (4mg/kg) sedation were used
508 for sample administration, collection of samples and conducting image collections. Analgesics
509 were used when determined appropriate by veterinary medical staff. Monkeys were fed Teklad
510 monkey chow supplemented with fresh fruit or vegetables and water ad libitum.
511 Rhesus macaques (n=8 main study + 4 separate non-concomitant study) were infected with 300
512 $TCID_{50}$ of the barcoded SIVmac239M2 stock intravenously and ART (Tenofovir [PMPA],
513 Emtricitabine [FTC] and Dolutegravir [DTG]) was initiated on week 6 pi. Galunisertib treatment

514 was initiated on week 35 p.i. Powder (MedChemExpress – MCE, NJ, USA) was dissolved in
515 water and given orally in a treat twice daily at 20mg/kg. 4 cycles of 2 weeks daily treatment with
516 2 weeks wash out period were performed. Macaques 08M156 and A6X003 were given the rhesus
517 recombinant antibody (rhesus/human chimeric) anti-PD1 antibody [NIVOR4LALA; comprising
518 silenced rhesus IgG4k constant regions and variable regions from anti-human PD-1, nivolumab;
519 non-human primates reagents resource, NHPRR.
520 Blood viral load was monitored biweekly before and during ART and every 3-4 days during
521 Galunisertib treatment. Colorectal biopsies and LN FNA were collected before and after
522 galunisertib treatment. ART was terminated 3 weeks after the last galunisertib dose and
523 euthanasia and necropsy to harvest tissues were performed at week 58 post infection, tissues
524 samples were flash frozen, fixed in OCT or Z-fix.
525
526 **Plasma and Tissue SIV Viral loads (VL)**
527 Blood was collected in EDTA tubes and plasma was separated by density gradient centrifugation
528 and used for the determination of plasma VL by SIVgag qRT-PCR at NIRC or at Leidos
529 (Quantitative Molecular Diagnostics Core, AIDS and Cancer Virus Program Frederick National
530 Laboratory). Tissue VL from snap frozen PBMC pellets, colorectal biopsies and LN FNA were
531 performed as described in (*73*). SIV-TILDA was performed on freshly stored PBMC before cycle
532 1 and at the end of cycle 4 of galunisertib by Accelevir, Baltimore, MD.
533
534 **ImmunoPET/CT**
535 ImmunoPET/CT for mapping SIV signals in total body scans were conducted in part as reported
536 previously(*42*). The probe consisted of primatized p7D3 anti-env F(ab)'2 coupled with the chelator
537 DOTA and labeled with Cu^{64} just prior to administration to the animals. For probe administration,
538 the animals were sedated, and a venous catheter was placed into an arm of leg vein to minimize
539 bleeding of the probe into the tissue surrounding the site of injection. The probe for each animal

540 consisted of ~1mg of the p7D3 F(ab)'2 labeled with 2-3 mCi of ^{64}Cu. After injection, the animals
541 were allowed to recuperate in their cage until the next day. At 24 hours, the animals were again
542 anesthetized with Telazol and the macaque's body was immobilized in dorsal recumbency on the
543 scanner table. Scans were conducted in a Phillips Gemini TF64 scanner. The final CT image was
544 compiled from 200 to 300 slices, depending on macaque size.
545 PET Image analysis was performed using the MIM software. PET/CT fusions were generated
546 scaled according to calculated Standardized Uptake Values (SUV). The SUV scale for the PET
547 scans was selected based on the overall signal intensity of the PET scans (whole body), and the
548 CT scale was selected for optimal visibility of the tissues. All images and maximum image
549 projections (MIP) were set to the same0-1.5 scale for visual comparisons. Additional details on
550 MIM analysis are described in Supplemental Methods.
551
552 **Cell isolation, flow cytometry staining, classical and high-dimensional analysis**
553 Colorectal biopsy tissues were isolated by enzymatic digestion while LN biopsies were passed
554 through a 70μm cell strainer as described in(*42*). Isolated cells were phenotyped with panels listed
555 in Supplemental Table S4. FlowJo vs 10.8 was use for both classical and high-dimesional
556 analysis. PeacoQC, FlowtSNE and FlowSOM plug-ins were used with default settings. SwiftReg
557 was used for normalization(*45*). More details on the staining procedures and analysis pipeline in
558 Supplemental Methods.
559
560 **Bulk and scRNAseq analysis**
561 For bulk RNAseq, snap frozen PBMC pellets from BC1, 1hr after first Gal dose and AC1 were
562 used for RNA extraction with the RNeasy kit with on column DNA digestion (Qiagen). Library
563 preparation was performed using TruSeq Stranded Total RNA with Ribo-Zero Globin and
564 sequencing was done with an Illumina HiSeq4000 with >20M reads/samples. Sequencing data
565 was demultiplexed and trimmed using Trimmomatic v0.36 to remove adapters and low-quality

566 reads. Trimmed reads were aligned to the Mmul10 reference genome and transcripts quantified
567 using the Hisat2-StringTie pipeline(*74*). Differential gene expression analysis using the quantified
568 gene transcripts was performed with DESeq2 R package(*75*) comparing the samples attained
569 before and after galunisertib treatment and controlling for intra-animal autocorrelation.
570 Differentially expressed genes (DEGs) were analyzed by functional enrichment analysis and gene
571 set enrichment analysis (GSEA) to identify specific pathways and molecular processes altered by
572 galunisertib.
573 The Parse pipeline and Partek software were used for scRNAseq analysis. For bulk RNAseq
574 features with <100 counts were removed, data normalized and DESeq2 was used to obtain a
575 DEG list. Genes with a false discovery rate (FDR)-adjusted p-value ≤0.05 and absolute $\log_2$ fold-
576 change (FC) (compared to BC1) above 2 were defined as significantly differentially expressed
577 (DEG). For scRNAseq analysis cells isolated from lymph nodes before (BC1) and after (AC1)
578 galunisertib were fixed with the Parse fixation kit, barcoded and sequenced at the NUseq Core.
579 The Partek software was used for scRNAseq analysis. Cells with 400-8000 features, excluding
580 features with 0 reads in >99.99 cells, were included. Scran deconvolution was used for
581 normalization and cell classification was based on gene expression. Hurdle models were used to
582 compare DEGs in each cell subset before and after galunisertib. See supplemental methods for
583 a detailed description of scRNAseq analysis and additional control analysis using Seurat R
584 package with more stringent QC cut-offs and SCTransform normalization.
585
586 **Plasma cytokines and T cell responses**
587 Cytokines in plasma (at 1:2 dilution) were measured using the NHP Cytokine 24-Plex kit by Meso
588 Scale Diagnostics (MSD) according to manufacturer instructions. Frozen PBMC collected at week
589 6 post-infection (pre-ART), right before the first galunisertib administration (BC1), at the end of
590 cycle 1 (AC1) and at the end of cycle 3 (AC3) were thawed in AIM V medium (Thermo Fisher)
591 with benzonase (Sigma) and plated on a FluoroSpot (CTL) plate pre-activated with 70% Ethanol

592 and IFN-γ, TNF-α and IL-2 capture solution. Gag, pol, and env 15-mer peptides (NIH AIDS
593 Reagents program) were prepared at two times the final concentration of 2.5µg/ml with co-
594 stimulatory reagents anti-CD28 10µg/ml and anti-CD49d 10µg/ml and added to the cells in CTL-
595 Test™ Medium. Parallel positive control of PMA (20ng/mL) and ionomycin (200ng/mL) or mock
596 DMSO solution was also plated with the stimulatory reagents. PBMCs were added at 300,000
597 cells per well. After 24hrs, the plate was washed, and incubated with detection and tertiary
598 solutions and shipped to CTL for scanning and QC.
599
600 **Statistics**
601 GraphPad Prism v10, R and Python were used for statistical analysis and data visualization.
602 Wilcoxon matched-pairs test and repeated measures ANOVA or mixed effect analysis (when the
603 data set had missing data) were used to compare the different virological and immunological
604 variables between baseline (BC1) and a single or multiple post-galunisertib time points. In Prism
605 the mixed model uses a compound symmetry covariance matrix, and is fit using Restricted
606 Maximum Likelihood (REML). Cytokine data from MSD assay were first Log transformed, then
607 normalized by subcolumn/factor in percentage with 0% as smallest value and 100% larger value
608 in each dataset. Each factor was analyzed separately with ANOVA for repeated measures and
609 Dunn's multiple comparison's post-hoc test and together by principal component analysis (PCA).
610 Holm-Sidak test was used for multiple comparison correction in all cases, but FlowSOM cluster
611 comparison where the FDR method was used. Pearson r coefficient was calculated for pairwise
612 tests of association in a correlation matrix with selected variables. For RNAseq analysis see
613 above and supplemental methods. For viral population analysis, Shannon Entropy of the viral
614 barcodes present in each sample was used to measure the diversity of the viral populations (see
615 supplemental Methods). Chi-squared tests were used in R to compare barcode composition
616 between before and after cycle time points within a tissue/macaque using paired barcode relative
617 frequencies. Unless otherwise specified p-value<0.05 was considered statistically significant.

618

619 **Data Availability Statement**

620 RNA sequencing data originating from this study have been deposited in NCBI GEO under the

621 accession code: GSE244871 For reviewers:

622 https://www.ncbi.nlm.nih.gov/geo/query/acc.cgi?acc=GSE244871 Enter token afmricsirpmlzul

623 into the box.

624 **LIST OF SUPPLEMENTARY MATERIALS**

625 Supplementary Methods

626 Supplementary Figure Fig. S1 to S17

627 Supplementary Table S1 to S6

628 Movies S1 to S10

629 **Acknowledgements**

630 **General:** We are thankful to Jorge Carrasquillo, Professor of Radiology (Weill Cornell) and
631 nuclear medicine specialist for helping us with the analysis and iinterpretation of the PET/CT
632 images. We acknowledge the helpful staff at the New Iberia Research Center as well as the help
633 of Dr. Suchitra Swaminathan and the rest of the staff of the Flow Cytometry Core Facility at the
634 Robert H. Lurie Comprehensive Cancer Center of Northwestern University in Chicago. Moreover,
635 we thank the staff of the NUseq Core at Northwestern, and in particular Dr. Ching Man Wai and
636 Matthew Schipma for the help with RNAseq data. Finally, we thank Dr. Lifson and the Leidos staff
637 for viral load measurements as well as Dr. Laird at Accelevir for providing SIV-TILDA results in a
638 timely manner. The content of this publication does not necessarily reflect the views or policies of
639 the Department of Health and Human Services, nor does mention of trade names, commercial
640 products, or organizations imply endorsement by the U.S. Government.

641 **Funding:** This project has been funded by National Institutes of Health grant R56AI157822 to Dr.
642 Martinelli, the resource for NHP immune reagents to Dr. Villinger (R24 OD010947) for probe
643 productions and in part with federal funds from the National Cancer Institute, National Institutes
644 of Health, under Contract No. 75N91019D00024/HHSN261201500003I. The Lurie Cancer Center
645 is supported in part by an NCI Cancer Center Support Grant #P30 CA060553.

646 **Authors contributions:** EM conceptualized the studies; JK performed and analyzed flow
647 cytometry and immunePET/CT data; DB, MA, DF and SA collected and processed macaque
648 samples; MRH generated vRNA/DNA and Elispot data; RC and MV analyzed Treg/Tfh; YT and
649 TJH contributed to immunePET/CT analysis; EG, YG and EM analyzed RNAseq data; CMF, BK
650 and RLR analyzed barcode data; JA, CC, FV and EM interpreted the data and wrote the
651 manuscript.

652 **Competing interests:** The authors declare no competing interests.

Data and material availability: All data needed to evaluate the conclusions in the paper are included in the manuscript and/or the supplemental material. Transcriptional profiling data (raw RNAseq data) will be uploaded to GEO.

REFERENCES

1. P. Gantner, S. Buranapraditkun, A. Pagliuzza, C. Dufour, M. Pardons, J. L. Mitchell, E. Kroon, C. Sacdalan, N. Tulmethakaan, S. Pinyakorn, M. L. Robb, N. Phanuphak, J. Ananworanich, D. Hsu, S. Vasan, L. Trautmann, R. Fromentin, N. Chomont, HIV rapidly targets a diverse pool of CD4(+) T cells to establish productive and latent infections. *Immunity* **56**, 653-668 e655 (2023).
2. J. B. Whitney, A. L. Hill, S. Sanisetty, P. Penaloza-MacMaster, J. Liu, M. Shetty, L. Parenteau, C. Cabral, J. Shields, S. Blackmore, J. Y. Smith, A. L. Brinkman, L. E. Peter, S. I. Mathew, K. M. Smith, E. N. Borducchi, D. I. Rosenbloom, M. G. Lewis, J. Hattersley, B. Li, J. Hesselgesser, R. Geleziunas, M. L. Robb, J. H. Kim, N. L. Michael, D. H. Barouch, Rapid seeding of the viral reservoir prior to SIV viraemia in rhesus monkeys. *Nature* **512**, 74-77 (2014).
3. D. Persaud, Y. Zhou, J. M. Siliciano, R. F. Siliciano, Latency in human immunodeficiency virus type 1 infection: no easy answers. *J Virol* **77**, 1659-1665 (2003).
4. D. M. Margolis, N. M. Archin, Proviral Latency, Persistent Human Immunodeficiency Virus Infection, and the Development of Latency Reversing Agents. *The Journal of infectious diseases* **215**, S111-S118 (2017).
5. T. A. Wagner, S. McLaughlin, K. Garg, C. Y. Cheung, B. B. Larsen, S. Styrchak, H. C. Huang, P. T. Edlefsen, J. I. Mullins, L. M. Frenkel, HIV latency. Proliferation of cells with HIV integrated into cancer genes contributes to persistent infection. *Science* **345**, 570-573 (2014).
6. F. Maldarelli, X. Wu, L. Su, F. R. Simonetti, W. Shao, S. Hill, J. Spindler, A. L. Ferris, J. W. Mellors, M. F. Kearney, J. M. Coffin, S. H. Hughes, HIV latency. Specific HIV integration sites are linked to clonal expansion and persistence of infected cells. *Science* **345**, 179-183 (2014).
7. L. B. Cohn, I. T. Silva, T. Y. Oliveira, R. A. Rosales, E. H. Parrish, G. H. Learn, B. H. Hahn, J. L. Czartoski, M. J. McElrath, C. Lehmann, F. Klein, M. Caskey, B. D. Walker, J. D. Siliciano, R. F. Siliciano, M. Jankovic, M. C. Nussenzweig, HIV-1 integration landscape during latent and active infection. *Cell* **160**, 420-432 (2015).
8. K. B. Einkauf, M. R. Osborn, C. Gao, W. Sun, X. Sun, X. Lian, E. M. Parsons, G. T. Gladkov, K. W. Seiger, J. E. Blackmer, C. Jiang, S. A. Yukl, E. S. Rosenberg, X. G. Yu, M. Lichterfeld, Parallel analysis of transcription, integration, and sequence of single HIV-1 proviruses. *Cell* **185**, 266-282 e215 (2022).
9. X. Lian, K. W. Seiger, E. M. Parsons, C. Gao, W. Sun, G. T. Gladkov, I. C. Roseto, K. B. Einkauf, M. R. Osborn, J. M. Chevalier, C. Jiang, J. Blackmer, M. Carrington, E. S. Rosenberg, M. M. Lederman, D. K. McMahon, R. J. Bosch, J. M. Jacobson, R. T. Gandhi, M. J. Peluso, T. W. Chun, S. G. Deeks, X. G. Yu, M. Lichterfeld, Progressive transformation of the HIV-1

694 reservoir cell profile over two decades of antiviral therapy. *Cell Host Microbe* **31**, 83-96
695 e85 (2023).
696 10. V. Singh, A. Dashti, M. Mavigner, A. Chahroudi, Latency Reversal 2.0: Giving the Immune
697 System a Seat at the Table. *Curr HIV/AIDS Rep* **18**, 117-127 (2021).
698 11. E. Abner, A. Jordan, HIV "shock and kill" therapy: In need of revision. *Antiviral Res* **166**, 19-
699 34 (2019).
700 12. A. Ait-Ammar, A. Kula, G. Darcis, R. Verdikt, S. De Wit, V. Gautier, P. W. G. Mallon, A.
701 Marcello, O. Rohr, C. Van Lint, Current Status of Latency Reversing Agents Facing the
702 Heterogeneity of HIV-1 Cellular and Tissue Reservoirs. *Frontiers in microbiology* **10**, 3060
703 (2019).
704 13. S. A. Yukl, P. Kaiser, P. Kim, S. Telwatte, S. K. Joshi, M. Vu, H. Lampiris, J. K. Wong, HIV latency
705 in isolated patient CD4(+) T cells may be due to blocks in HIV transcriptional elongation,
706 completion, and splicing. *Sci Transl Med* **10**, (2018).
707 14. J. D. Siliciano, R. F. Siliciano, Low Inducibility of Latent Human Immunodeficiency Virus
708 Type 1 Proviruses as a Major Barrier to Cure. *J Infect Dis* **223**, 13-21 (2021).
709 15. Y. C. Ho, L. Shan, N. N. Hosmane, J. Wang, S. B. Laskey, D. I. Rosenbloom, J. Lai, J. N.
710 Blankson, J. D. Siliciano, R. F. Siliciano, Replication-competent noninduced proviruses in
711 the latent reservoir increase barrier to HIV-1 cure. *Cell* **155**, 540-551 (2013).
712 16. E. N. Borducchi, C. Cabral, K. E. Stephenson, J. Liu, P. Abbink, D. Ng'ang'a, J. P. Nkolola, A.
713 L. Brinkman, L. Peter, B. C. Lee, J. Jimenez, D. Jetton, J. Mondesir, S. Mojta, A.
714 Chandrashekar, K. Molloy, G. Alter, J. M. Gerold, A. L. Hill, M. G. Lewis, M. G. Pau, H.
715 Schuitemaker, J. Hesselgesser, R. Geleziunas, J. H. Kim, M. L. Robb, N. L. Michael, D. H.
716 Barouch, Ad26/MVA therapeutic vaccination with TLR7 stimulation in SIV-infected rhesus
717 monkeys. *Nature* **540**, 284-287 (2016).
718 17. C. C. Nixon, M. Mavigner, G. C. Sampey, A. D. Brooks, R. A. Spagnuolo, D. M. Irlbeck, C.
719 Mattingly, P. T. Ho, N. Schoof, C. G. Cammon, G. K. Tharp, M. Kanke, Z. Wang, R. A. Cleary,
720 A. A. Upadhyay, C. De, S. R. Wills, S. D. Falcinelli, C. Galardi, H. Walum, N. J. Schramm, J.
721 Deutsch, J. D. Lifson, C. M. Fennessey, B. F. Keele, S. Jean, S. Maguire, B. Liao, E. P. Browne,
722 R. G. Ferris, J. H. Brehm, D. Favre, T. H. Vanderford, S. E. Bosinger, C. D. Jones, J. P. Routy,
723 N. M. Archin, D. M. Margolis, A. Wahl, R. M. Dunham, G. Silvestri, A. Chahroudi, J. V. Garcia,
724 Systemic HIV and SIV latency reversal via non-canonical NF-kappaB signalling in vivo.
725 *Nature* **578**, 160-165 (2020).
726 18. D. O'Sullivan, The metabolic spectrum of memory T cells. *Immunol Cell Biol* **97**, 636-646
727 (2019).
728 19. J. M. Crater, D. F. Nixon, R. L. Furler O'Brien, HIV-1 replication and latency are balanced by
729 mTOR-driven cell metabolism. *Front Cell Infect Microbiol* **12**, 1068436 (2022).
730 20. E. Besnard, S. Hakre, M. Kampmann, H. W. Lim, N. N. Hosmane, A. Martin, M. C. Bassik, E.
731 Verschueren, E. Battivelli, J. Chan, J. P. Svensson, A. Gramatica, R. J. Conrad, M. Ott, W. C.
732 Greene, N. J. Krogan, R. F. Siliciano, J. S. Weissman, E. Verdin, The mTOR Complex Controls
733 HIV Latency. *Cell Host Microbe* **20**, 785-797 (2016).
734 21. H. J. Barbian, M. S. Seaton, S. D. Narasipura, J. Wallace, R. Rajan, B. E. Sha, L. Al-Harthi,
735 beta-catenin regulates HIV latency and modulates HIV reactivation. *PLoS Pathog* **18**,
736 e1010354 (2022).

737 22. F. Gounari, K. Khazaie, TCF-1: a maverick in T cell development and function. *Nat Immunol*
738 **23**, 671-678 (2022).
739 23. J. C. Valle-Casuso, M. Angin, S. Volant, C. Passaes, V. Monceaux, A. Mikhailova, K. Bourdic,
740 V. Avettand-Fenoel, F. Boufassa, M. Sitbon, O. Lambotte, M. I. Thoulouze, M. Muller-
741 Trutwin, N. Chomont, A. Saez-Cirion, Cellular Metabolism Is a Major Determinant of HIV-
742 1 Reservoir Seeding in CD4(+) T Cells and Offers an Opportunity to Tackle Infection. *Cell*
743 *Metab* **29**, 611-626 e615 (2019).
744 24. S. A. Oh, M. O. Li, TGF-beta: guardian of T cell function. *Journal of immunology* **191**, 3973-
745 3979 (2013).
746 25. S. S. Gabriel, C. Tsui, D. Chisanga, F. Weber, M. Llano-Leon, P. M. Gubser, L. Bartholin, F.
747 Souza-Fonseca-Guimaraes, N. D. Huntington, W. Shi, D. T. Utzschneider, A. Kallies,
748 Transforming growth factor-beta-regulated mTOR activity preserves cellular metabolism
749 to maintain long-term T cell responses in chronic infection. *Immunity* **54**, 1698-1714
750 e1695 (2021).
751 26. Y. Hu, W. H. Hudson, H. T. Kissick, C. B. Medina, A. P. Baptista, C. Ma, W. Liao, R. N. Germain,
752 S. J. Turley, N. Zhang, R. Ahmed, TGF-beta regulates the stem-like state of PD-1+ TCF-1+
753 virus-specific CD8 T cells during chronic infection. *J Exp Med* **219**, (2022).
754 27. C. Ma, N. Zhang, Transforming growth factor-beta signaling is constantly shaping memory
755 T-cell population. *Proc Natl Acad Sci U S A* **112**, 11013-11017 (2015).
756 28. S. Viel, A. Marcais, F. S. Guimaraes, R. Loftus, J. Rabilloud, M. Grau, S. Degouve, S. Djebali,
757 A. Sanlaville, E. Charrier, J. Bienvenu, J. C. Marie, C. Caux, J. Marvel, L. Town, N. D.
758 Huntington, L. Bartholin, D. Finlay, M. J. Smyth, T. Walzer, TGF-beta inhibits the activation
759 and functions of NK cells by repressing the mTOR pathway. *Sci Signal* **9**, ra19 (2016).
760 29. J. S. Delisle, M. Giroux, G. Boucher, J. R. Landry, M. P. Hardy, S. Lemieux, R. G. Jones, B. T.
761 Wilhelm, C. Perreault, The TGF-beta-Smad3 pathway inhibits CD28-dependent cell growth
762 and proliferation of CD4 T cells. *Genes Immun* **14**, 115-126 (2013).
763 30. G. M. Lewis, E. J. Wehrens, L. Labarta-Bajo, H. Streeck, E. I. Zuniga, TGF-beta receptor
764 maintains CD4 T helper cell identity during chronic viral infections. *J Clin Invest* **126**, 3799-
765 3813 (2016).
766 31. A. P. Nath, A. Braun, S. C. Ritchie, F. R. Carbone, L. K. Mackay, T. Gebhardt, M. Inouye,
767 Comparative analysis reveals a role for TGF-beta in shaping the residency-related
768 transcriptional signature in tissue-resident memory CD8+ T cells. *PLoS One* **14**, e0210495
769 (2019).
770 32. N. Zhang, M. J. Bevan, Transforming growth factor-beta signaling controls the formation
771 and maintenance of gut-resident memory T cells by regulating migration and retention.
772 *Immunity* **39**, 687-696 (2013).
773 33. T. Hirai, Y. Yang, Y. Zenke, H. Li, V. K. Chaudhri, J. S. De La Cruz Diaz, P. Y. Zhou, B. A. Nguyen,
774 L. Bartholin, C. J. Workman, D. W. Griggs, D. A. A. Vignali, H. Singh, D. Masopust, D. H.
775 Kaplan, Competition for Active TGFbeta Cytokine Allows for Selective Retention of
776 Antigen-Specific Tissue- Resident Memory T Cells in the Epidermal Niche. *Immunity* **54**,
777 84-98 e85 (2021).
778 34. C. Larson, B. Oronsky, C. A. Carter, A. Oronsky, S. J. Knox, D. Sher, T. R. Reid, TGF-beta: a
779 master immune regulator. *Expert Opin Ther Targets* **24**, 427-438 (2020).

35. S. Samer, Y. Thomas, M. Arainga, C. Carter, L. M. Shirreff, M. S. Arif, J. M. Avita, I. Frank, M. D. McRaven, C. T. Thuruthiyil, V. B. Heybeli, M. R. Anderson, B. Owen, A. Gaisin, D. Bose, L. M. Simons, J. F. Hultquist, J. Arthos, C. Cicala, I. Sereti, P. J. Santangelo, R. Lorenzo-Redondo, T. J. Hope, F. J. Villinger, E. Martinelli, Blockade of TGF-beta signaling reactivates HIV-1/SIV reservoirs and immune responses in vivo. *JCI Insight* **7**, (2022).
36. S. Bergstresser, D. A. Kulpa, TGF-beta Signaling Supports HIV Latency in a Memory CD4+ T Cell Based In Vitro Model. *Methods Mol Biol* **2407**, 69-79 (2022).
37. S. Chinnapaiyan, R. K. Dutta, M. Nair, H. S. Chand, I. Rahman, H. J. Unwalla, TGF-beta1 increases viral burden and promotes HIV-1 latency in primary differentiated human bronchial epithelial cells. *Scientific reports* **9**, 12552 (2019).
38. R. B. Holmgaard, D. A. Schaer, Y. Li, S. P. Castaneda, M. Y. Murphy, X. Xu, I. Inigo, J. Dobkin, J. R. Manro, P. W. Iversen, D. Surguladze, G. E. Hall, R. D. Novosiadly, K. A. Benhadji, G. D. Plowman, M. Kalos, K. E. Driscoll, Targeting the TGFbeta pathway with galunisertib, a TGFbetaRI small molecule inhibitor, promotes anti-tumor immunity leading to durable, complete responses, as monotherapy and in combination with checkpoint blockade. *J Immunother Cancer* **6**, 47 (2018).
39. D. Melisi, D. Y. Oh, A. Hollebecque, E. Calvo, A. Varghese, E. Borazanci, T. Macarulla, V. Merz, C. Zecchetto, Y. Zhao, I. Gueorguieva, M. Man, L. Gandhi, S. T. Estrem, K. A. Benhadji, M. C. Lanasa, E. Avsar, S. C. Guba, R. Garcia-Carbonero, Safety and activity of the TGFbeta receptor I kinase inhibitor galunisertib plus the anti-PD-L1 antibody durvalumab in metastatic pancreatic cancer. *J Immunother Cancer* **9**, (2021).
40. A. Wick, A. Desjardins, C. Suarez, P. Forsyth, I. Gueorguieva, T. Burkholder, A. L. Cleverly, S. T. Estrem, S. Wang, M. M. Lahn, S. C. Guba, D. Capper, J. Rodon, Phase 1b/2a study of galunisertib, a small molecule inhibitor of transforming growth factor-beta receptor I, in combination with standard temozolomide-based radiochemotherapy in patients with newly diagnosed malignant glioma. *Invest New Drugs* **38**, 1570-1579 (2020).
41. P. J. Santangelo, K. A. Rogers, C. Zurla, E. L. Blanchard, S. Gumber, K. Strait, F. Connor-Stroud, D. M. Schuster, P. K. Amancha, J. J. Hong, S. N. Byrareddy, J. A. Hoxie, B. Vidakovic, A. A. Ansari, E. Hunter, F. Villinger, Whole-body immunoPET reveals active SIV dynamics in viremic and antiretroviral therapy-treated macaques. *Nat Methods* **12**, 427-432 (2015).
42. S. Samer, Y. Thomas, M. Araínga, C. Carter, L. Shirreff, M. Arif, J. Avita, I. Frank, M. McRaven, C. Thuruthiyil, V. Heybeli, M. Anderson, B. Owen, A. Gaisin, D. Bose, L. Simons, J. Hultquist, J. Arthos, C. Cicala, I. Sereti, P. Santangelo, R. Lorenzo-Redondo, T. Hope, F. Villinger, E. Martinelli, Blockade of TGF-β signaling reactivates HIV-1/SIV reservoirs and immune responses in vivo. *bioRxiv*, 2022.2005.2013.489595 (2022).
43. S. J. Im, B. T. Konieczny, W. H. Hudson, D. Masopust, R. Ahmed, PD-1+ stemlike CD8 T cells are resident in lymphoid tissues during persistent LCMV infection. *Proc Natl Acad Sci U S A* **117**, 4292-4299 (2020).
44. S. Van Gassen, B. Callebaut, M. J. Van Helden, B. N. Lambrecht, P. Demeester, T. Dhaene, Y. Saeys, FlowSOM: Using self-organizing maps for visualization and interpretation of cytometry data. *Cytometry A* **87**, 636-645 (2015).
45. J. A. Rebhahn, S. A. Quataert, G. Sharma, T. R. Mosmann, SwiftReg cluster registration automatically reduces flow cytometry data variability including batch effects. *Commun Biol* **3**, 218 (2020).

824 46. M. J. Blackburn, M. Zhong-Min, F. Caccuri, K. McKinnon, L. Schifanella, Y. Guan, G. Gorini,
825 D. Venzon, C. Fenizia, N. Binello, S. N. Gordon, C. J. Miller, G. Franchini, M. Vaccari,
826 Regulatory and Helper Follicular T Cells and Antibody Avidity to Simian Immunodeficiency
827 Virus Glycoprotein 120. *J Immunol* **195**, 3227-3236 (2015).
828 47. S. Helmold Hait, D. A. Vargas-Inchaustegui, T. Musich, V. Mohanram, I. Tuero, D. J. Venzon,
829 J. Bear, M. Rosati, M. Vaccari, G. Franchini, B. K. Felber, G. N. Pavlakis, M. Robert-Guroff,
830 Early T Follicular Helper Cell Responses and Germinal Center Reactions Are Associated
831 with Viremia Control in Immunized Rhesus Macaques. *J Virol* **93**, (2019).
832 48. Y. Zhou, B. Zhou, L. Pache, M. Chang, A. H. Khodabakhshi, O. Tanaseichuk, C. Benner, S. K.
833 Chanda, Metascape provides a biologist-oriented resource for the analysis of systems-
834 level datasets. *Nat Commun* **10**, 1523 (2019).
835 49. Z. Qiu, T. H. Chu, B. S. Sheridan, TGF-beta: Many Paths to CD103(+) CD8 T Cell Residency.
836 *Cells* **10**, (2021).
837 50. H. S. Lim, P. Qiu, Quantifying Cell-Type-Specific Differences of Single-Cell Datasets Using
838 Uniform Manifold Approximation and Projection for Dimension Reduction and Shapley
839 Additive exPlanations. *J Comput Biol* **30**, 738-750 (2023).
840 51. X. Liao, N. Sharma, F. Kapadia, G. Zhou, Y. Lu, H. Hong, K. Paruchuri, G. H. Mahabeleshwar,
841 E. Dalmas, N. Venteclef, C. A. Flask, J. Kim, B. W. Doreian, K. Q. Lu, K. H. Kaestner, A. Hamik,
842 K. Clement, M. K. Jain, Kruppel-like factor 4 regulates macrophage polarization. *J Clin*
843 *Invest* **121**, 2736-2749 (2011).
844 52. M. A. Moso, J. L. Anderson, S. Adikari, L. R. Gray, G. Khoury, J. J. Chang, J. C. Jacobson, A.
845 M. Ellett, W. J. Cheng, S. Saleh, J. J. Zaunders, D. F. J. Purcell, P. U. Cameron, M. J. Churchill,
846 S. R. Lewin, H. K. Lu, HIV latency can be established in proliferating and nonproliferating
847 resting CD4+ T cells in vitro: implications for latency reversal. *AIDS* **33**, 199-209 (2019).
848 53. J. Neidleman, X. Luo, J. Frouard, G. Xie, F. Hsiao, T. Ma, V. Morcilla, A. Lee, S. Telwatte, R.
849 Thomas, W. Tamaki, B. Wheeler, R. Hoh, M. Somsouk, P. Vohra, J. Milush, K. S. James, N.
850 M. Archin, P. W. Hunt, S. G. Deeks, S. A. Yukl, S. Palmer, W. C. Greene, N. R. Roan,
851 Phenotypic analysis of the unstimulated in vivo HIV CD4 T cell reservoir. *Elife* **9**, (2020).
852 54. A. Chitrakar, M. Sanz, S. B. Maggirwar, N. Soriano-Sarabia, HIV Latency in Myeloid Cells:
853 Challenges for a Cure. *Pathogens* **11**, (2022).
854 55. E. L. Pearce, Metabolism in T cell activation and differentiation. *Curr Opin Immunol* **22**,
855 314-320 (2010).
856 56. H. Valdez, M. M. Lederman, Cytokines and cytokine therapies in HIV infection. *AIDS Clin*
857 *Rev*, 187-228 (1997).
858 57. R. J. Salmond, Regulation of T Cell Activation and Metabolism by Transforming Growth
859 Factor-Beta. *Biology (Basel)* **12**, (2023).
860 58. S. Regis, A. Dondero, F. Caliendo, C. Bottino, R. Castriconi, NK Cell Function Regulation by
861 TGF-beta-Induced Epigenetic Mechanisms. *Front Immunol* **11**, 311 (2020).
862 59. V. Zaiatz-Bittencourt, D. K. Finlay, C. M. Gardiner, Canonical TGF-beta Signaling Pathway
863 Represses Human NK Cell Metabolism. *J Immunol* **200**, 3934-3941 (2018).
864 60. L. Das, A. D. Levine, TGF-beta inhibits IL-2 production and promotes cell cycle arrest in
865 TCR-activated effector/memory T cells in the presence of sustained TCR signal
866 transduction. *J Immunol* **180**, 1490-1498 (2008).
867 61. W. Chen, TGF-beta Regulation of T Cells. *Annu Rev Immunol* **41**, 483-512 (2023).

868 62. T. Yamazaki, A. J. Gunderson, M. Gilchrist, M. Whiteford, M. X. Kiely, A. Hayman, D. O'Brien,
869 R. Ahmad, J. V. Manchio, N. Fox, K. McCarty, M. Phillips, E. Brosnan, G. Vaccaro, R. Li, M.
870 Simon, E. Bernstein, M. McCormick, L. Yamasaki, Y. Wu, A. Drokin, T. Carnahan, Y. To, W. L.
871 Redmond, B. Lee, J. Louie, E. Hansen, M. C. Solhjem, J. Cramer, W. J. Urba, M. J. Gough, M.
872 R. Crittenden, K. H. Young, Galunisertib plus neoadjuvant chemoradiotherapy in patients
873 with locally advanced rectal cancer: a single-arm, phase 2 trial. *Lancet Oncol* **23**, 1189-
874 1200 (2022).
875 63. J. J. Harding, R. K. Do, A. Yaqubie, A. Cleverly, Y. Zhao, I. Gueorguieva, M. Lahn, K. A.
876 Benhadji, R. K. Kelley, G. K. Abou-Alfa, Phase 1b study of galunisertib and ramucirumab in
877 patients with advanced hepatocellular carcinoma. *Cancer Med* **10**, 3059-3067 (2021).
878 64. R. K. Kelley, E. Gane, E. Assenat, J. Siebler, P. R. Galle, P. Merle, I. O. Hourmand, A. Cleverly,
879 Y. Zhao, I. Gueorguieva, M. Lahn, S. Faivre, K. A. Benhadji, G. Giannelli, A Phase 2 Study of
880 Galunisertib (TGF-beta1 Receptor Type I Inhibitor) and Sorafenib in Patients With
881 Advanced Hepatocellular Carcinoma. *Clin Transl Gastroenterol* **10**, e00056 (2019).
882 65. D. Melisi, R. Garcia-Carbonero, T. Macarulla, D. Pezet, G. Deplanque, M. Fuchs, J. Trojan,
883 H. Oettle, M. Kozloff, A. Cleverly, C. Smith, S. T. Estrem, I. Gueorguieva, M. M. F. Lahn, A.
884 Blunt, K. A. Benhadji, J. Tabernero, Galunisertib plus gemcitabine vs. gemcitabine for first-
885 line treatment of patients with unresectable pancreatic cancer. *Br J Cancer* **119**, 1208-
886 1214 (2018).
887 66. T. E. Walshe, M. Saint-Geniez, A. S. Maharaj, E. Sekiyama, A. E. Maldonado, P. A. D'Amore,
888 TGF-beta is required for vascular barrier function, endothelial survival and homeostasis of
889 the adult microvasculature. *PLoS One* **4**, e5149 (2009).
890 67. P. J. Santangelo, C. Cicala, S. N. Byrareddy, K. T. Ortiz, D. Little, K. E. Lindsay, S. Gumber, J.
891 J. Hong, K. Jelicic, K. A. Rogers, C. Zurla, F. Villinger, A. A. Ansari, A. S. Fauci, J. Arthos, Early
892 treatment of SIV+ macaques with an alpha(4)beta(7) mAb alters virus distribution and
893 preserves CD4(+) T cells in later stages of infection. *Mucosal Immunol* **11**, 932-946 (2018).
894 68. E. J. Fray, F. Wu, F. R. Simonetti, C. Zitzmann, N. Sambaturu, C. Molina-Paris, A. M. Bender,
895 P. T. Liu, J. D. Ventura, R. W. Wiseman, D. H. O'Connor, R. Geleziunas, T. Leitner, R. M.
896 Ribeiro, A. S. Perelson, D. H. Barouch, J. D. Siliciano, R. F. Siliciano, Antiretroviral therapy
897 reveals triphasic decay of intact SIV genomes and persistence of ancestral variants. *Cell*
898 *Host Microbe* **31**, 356-372 e355 (2023).
899 69. G. Escobar, D. Mangani, A. C. Anderson, T cell factor 1: A master regulator of the T cell
900 response in disease. *Sci Immunol* **5**, (2020).
901 70. R. L. Rutishauser, C. D. T. Deguit, J. Hiatt, F. Blaeschke, T. L. Roth, L. Wang, K. A. Raymond,
902 C. E. Starke, J. C. Mudd, W. Chen, C. Smullin, R. Matus-Nicodemos, R. Hoh, M. Krone, F. M.
903 Hecht, C. D. Pilcher, J. N. Martin, R. A. Koup, D. C. Douek, J. M. Brenchley, R. P. Sekaly, S. K.
904 Pillai, A. Marson, S. G. Deeks, J. M. McCune, P. W. Hunt, TCF-1 regulates HIV-specific CD8+
905 T cell expansion capacity. *JCI Insight* **6**, (2021).
906 71. Y. S. Choi, J. A. Gullicksrud, S. Xing, Z. Zeng, Q. Shan, F. Li, P. E. Love, W. Peng, H. H. Xue, S.
907 Crotty, LEF-1 and TCF-1 orchestrate T(FH) differentiation by regulating differentiation
908 circuits upstream of the transcriptional repressor Bcl6. *Nat Immunol* **16**, 980-990 (2015).
909 72. S. G. Zheng, J. Wang, P. Wang, J. D. Gray, D. A. Horwitz, IL-2 is essential for TGF-beta to
910 convert naive CD4+CD25- cells to CD25+Foxp3+ regulatory T cells and for expansion of
911 these cells. *J Immunol* **178**, 2018-2027 (2007).

73. I. Frank, M. Cigoli, M. S. Arif, M. D. Fahlberg, S. Maldonado, G. Calenda, A. Pegu, E. S. Yang, R. Rawi, G. Y. Chuang, H. Geng, C. Liu, T. Zhou, P. D. Kwong, J. Arthos, C. Cicala, B. F. Grasperge, J. L. Blanchard, A. Gettie, C. M. Fennessey, B. F. Keele, M. Vaccari, T. J. Hope, A. S. Fauci, J. R. Mascola, E. Martinelli, Blocking alpha4beta7 integrin delays viral rebound in SHIVSF162P3-infected macaques treated with anti-HIV broadly neutralizing antibodies. *Sci Transl Med* **13**, (2021).
74. M. Pertea, D. Kim, G. M. Pertea, J. T. Leek, S. L. Salzberg, Transcript-level expression analysis of RNA-seq experiments with HISAT, StringTie and Ballgown. *Nat Protoc* **11**, 1650-1667 (2016).
75. M. I. Love, W. Huber, S. Anders, Moderated estimation of fold change and dispersion for RNA-seq data with DESeq2. *Genome Biol* **15**, 550 (2014).

926 **FIGURES**

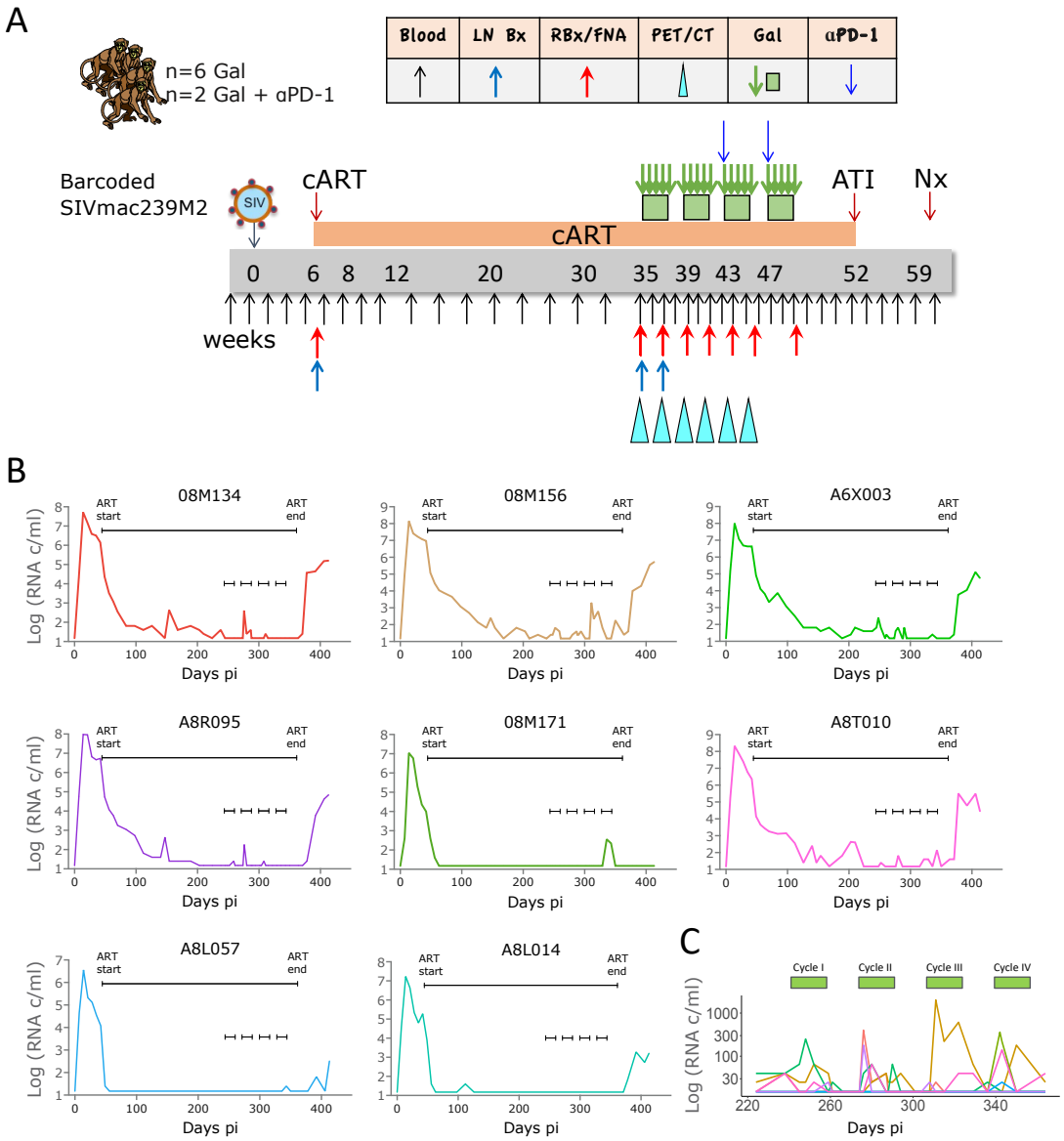

927 **Figure 1. Four 2-weeks cycles with galunisertib lead to viral reactivation in blood.** A)
928 Schematic representation of the study and sampling schedule B) Plasma VL in blood for each
929 macaque throughout the study. The longer black line indicates the period on ART, while the 4
930 small black lines indicate the start and end of each galunisertib cycle. C) Enlarged plasma VL for
931 all macaques during galunisertib therapy. Green bars indicate galunisertib cycles.

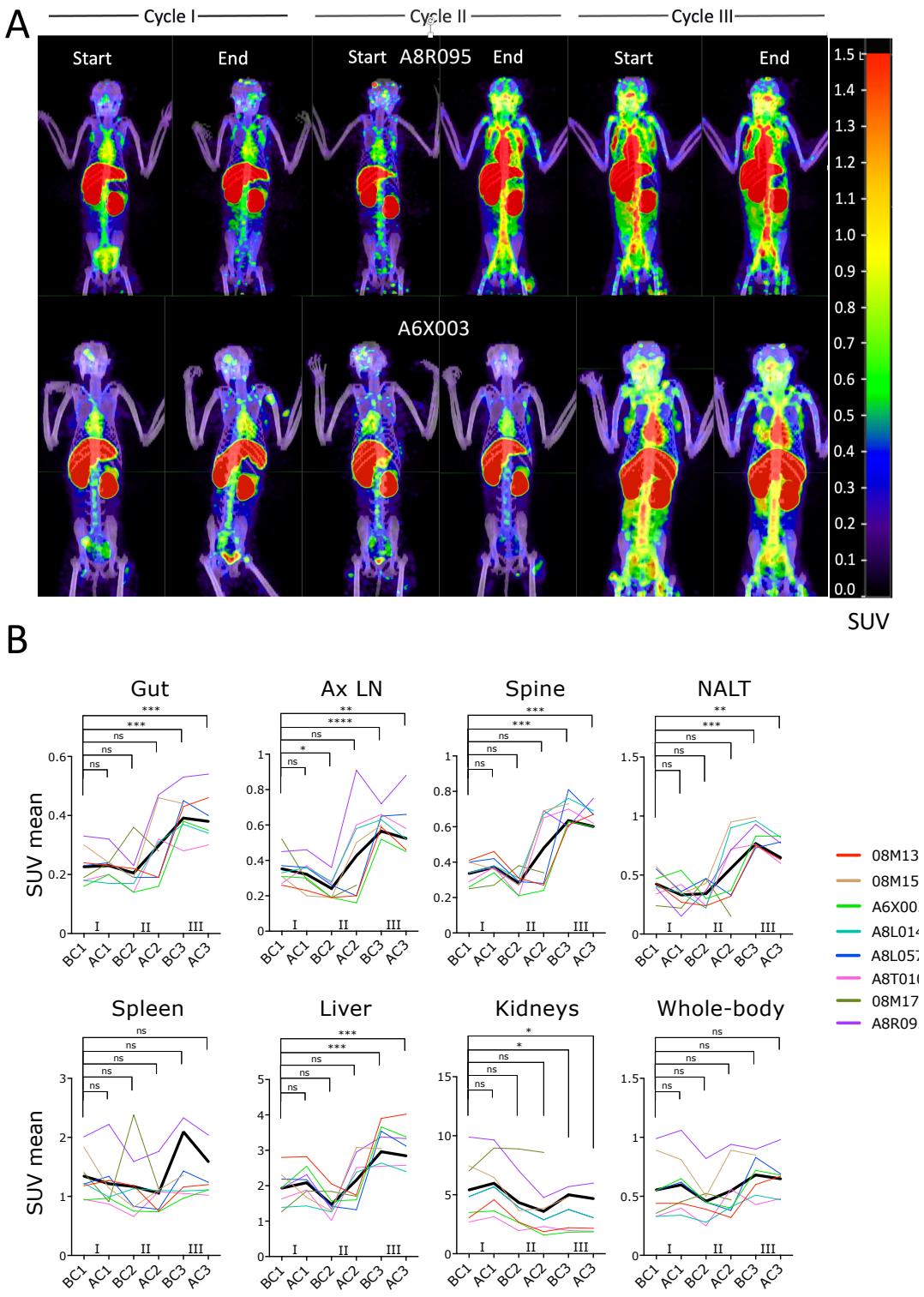

932 **Figure 2. Galunisertib leads to viral reactivation in tissues.** A) The ^{64}Cu-DOTA-Fab$_2$(7D3)

933 probe was injected ~24hrs before PET/CT scan before and at the end of each of the first 3

galunisertib cycles. Representative images from the maximum intensity projections (MIP) of fused PET and CT scans are show for a macaque with a major increase at the end of cycle 2 and one showing increase at the beginning of cycle 3. MIPs were generated using the MIM software, set to a numerical scale of 0-1.5 SUVbw and visualized with the *Rainbow* color scale. B) Mean SUV were calculated for each anatomical area and values analyzed with mixed-effect analysis. Thicker black line represents the mean. P–values were calculated for comparison of each time point with the before cycle 1 time point (BC1; AC1= after cycle 1, BC2= before cycle 2; AC2= after cycle 2; BC3= before cycle 3; AC3= after cycle 3; Holm-Sidak multiple comparison correction; *p≤0.05 **p≤0.01 ***p≤0.01)

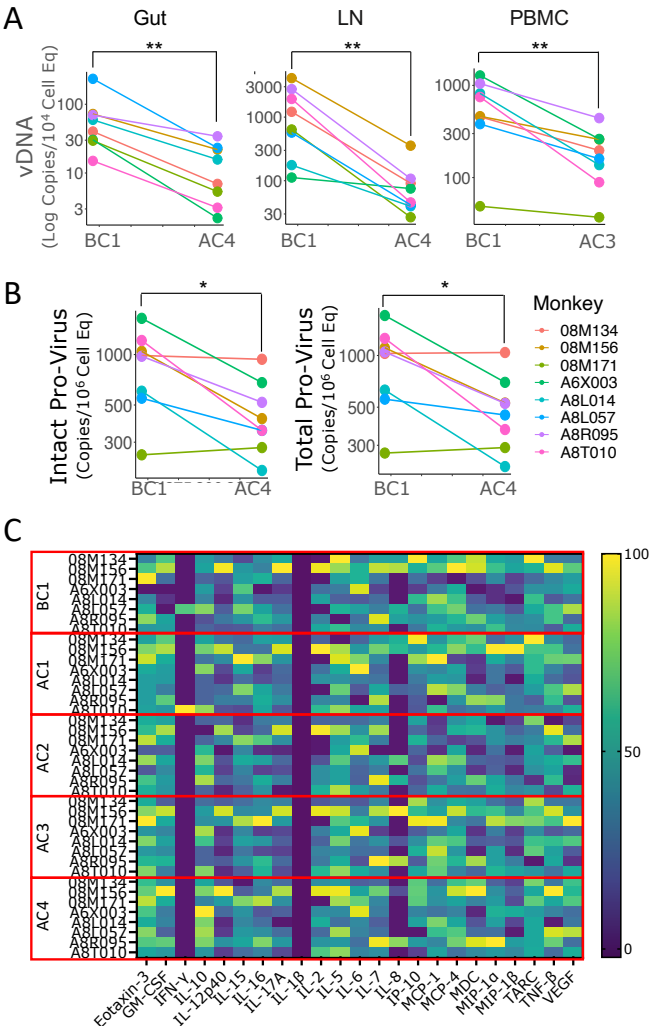

944 **Figure 3. Galunisertib decreases viral reservoir in absence of systemic inflammation.** A)
945 Levels of cell-associated (CA)-vDNA per cell equivalent are shown for the time point before cycle
946 1 (BC1) and at the end of cycle 3 (AC3) or 4 (AC4) for the respective tissues. B) IPDA data are
947 shown for intact and total provirus for BC1 and AC4 in PBMC. pvalues are shown for Wilcoxon
948 matched pair signed-rank non-parametric test (*$p \leq 0.05$ **$p \leq 0.01$ ***$p \leq 0.01$) C) Heat map of
949 cytokine concentration in plasma at the indicated time point are shown after Log transformation
950 and normalization. Statistical analysis was run on each factor separately and together (no
951 significant differences after multiple comparison adjustment).

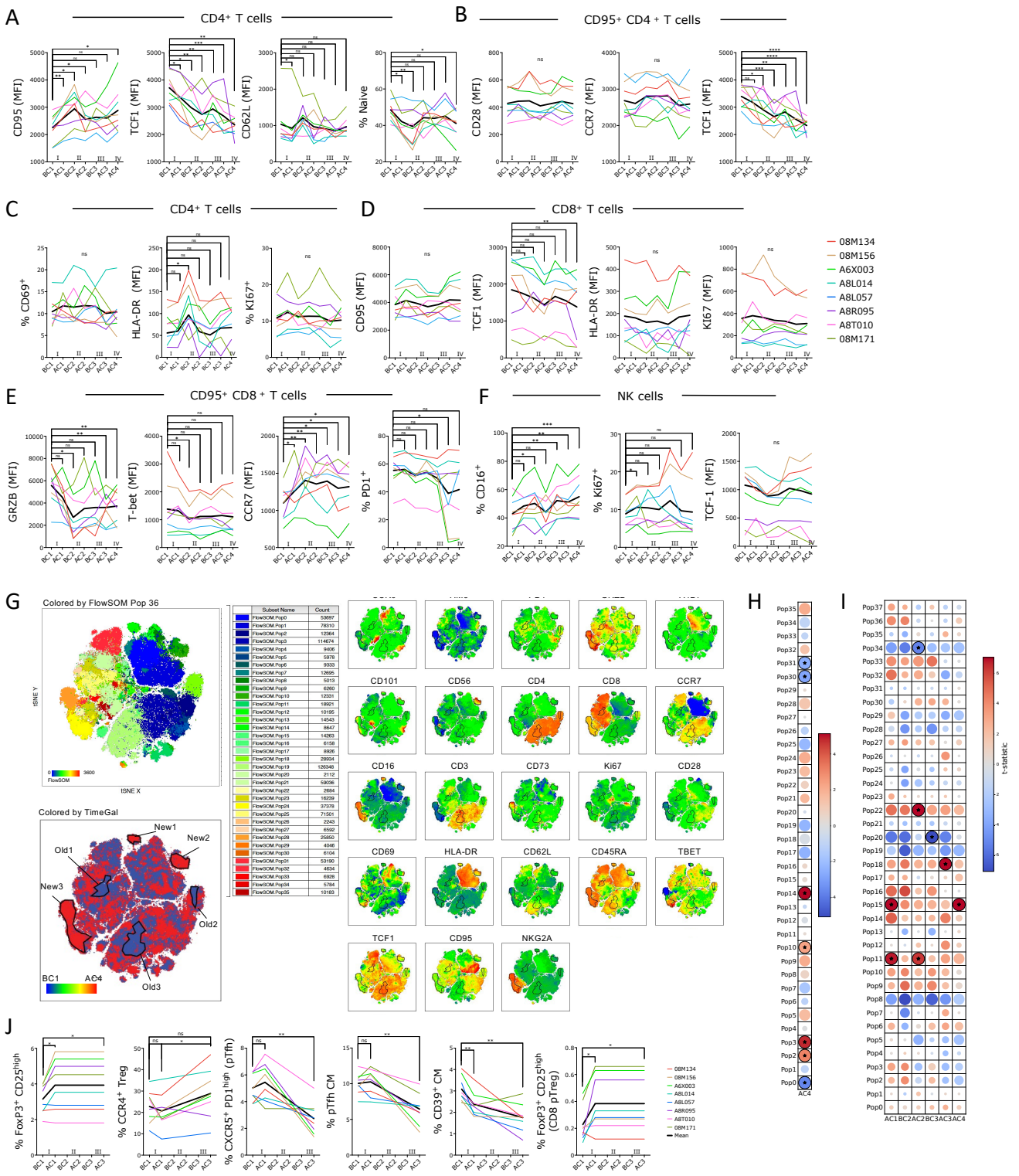
A
CD4+ T cells
CD95 (MFI)
TCF1 (MFI)
CD62L (MFI)
% Naive
B
CD95+ CD4 + T cells
CD28 (MFI)
CCR7 (MFI)
TCF1 (MFI)
C
CD4+ T cells
% CD69+
HLA-DR (MFI)
% Ki67+
D
CD8+ T cells
CD95 (MFI)
TCF1 (MFI)
HLA-DR (MFI)
Ki67 (MFI)
08M134
08M156
A6X003
A8L014
A8L057
A8R095
A8T010
08M171
E
CD95+ CD8 + T cells
GRZB (MFI)
T-bet (MFI)
CCR7 (MFI)
% PD1+
F
NK cells
% CD16+
% Ki67+
TCF-1 (MFI)
G
Colored by FlowSOM Pop 36
tSNE Y
tSNE X
FlowSOM
Colored by TimeGal
New1
New2
Old1
New3
Old2
Old3
BC1
AC4
CD101
CD56
CD4
CD8
CCR7
CD16
CD3
CD73
Ki67
CD28
CD69
HLA-DR
CD62L
CD45RA
TBET
TCF1
CD95
NKG2A
H
AC4
I
t-statistic
J
% FoxP3+ CD25high
% CCR4+ Treg
% CXCR5+ PD1high (pTfh)
% pTfh CM
% CD39+ CM
% FoxP3+ CD25high (CD8 pTreg)
08M134
08M156
A6X003
A8L014
A8L057
A8R095
A8T010
08M171
Mean

952

953 **Figure 4. Galunisertib leads toward effector in T and NK cells, increasing Treg and**
954 **decreasing Tfh frequencies.** A-F) Geometric mean fluorescent intensities (MFI) of each marker
955 and frequency of indicated subset within live, singlets $CD3^+$ $CD4^+$ T cells (A and C) or $CD3^+$ $CD4^+$
956 $CD95^+$ T cells (B) or $CD8^+$ or $CD8^+$ $CD95^+$ T cells or NK cells ($NKG2A^+$ $CD8^+$ $CD3^-$ cells) are
957 shown. Thick black line represents the mean. Changes from baseline (beginning of cycle 1, BC1)
958 are shown for graphs with at least 1 significant difference (Repeated measures ANOVA with Holm-
959 Sidak correction; *p≤0.05 **p≤0.01 ***p≤0.01). G) tSNE of lymphocyte, live, singlets events after
960 normalization for BC1 and AC4 (all 8 macaques) with FlowSOM 36 clusters overlaid on tSNE (top
961 left) or heatmap of each markers MFI (right) or heatmap of time point (blue is BC1 and red is AC4;
962 bottom left) is shown. 6 populations were manually gated on red or blue areas (red, New1-3 and
963 blue Old1-3). H) Bubble chart displaying changes from BC1 in AC4. Color is proportional to the
964 effect size and size to p-value (Wilcoxon sum rank non-parameter test). I) Bubble chart displaying
965 changes from BC1 in all time point (ANOVA repeated measures with Holm-Sidak correction;
966 *p≤0.05 **p≤0.01 ***p≤0.01). J) Frequency of indicated subset within live, singlets $CD3^+$ $CD4^+$ T
967 or $CD3^+$ $CD4^+$ $CD95^+$ $CD28^+$ T cells (CM=central memory) or within $CD3^+$ $CD8^+$ T cells. Changes
968 from baseline (BC1) are shown (ANOVA repeated measures with Holm-Sidak correction for
969 multiple comparisons; *p≤0.05 **p≤0.01 ***p≤0.01).
970

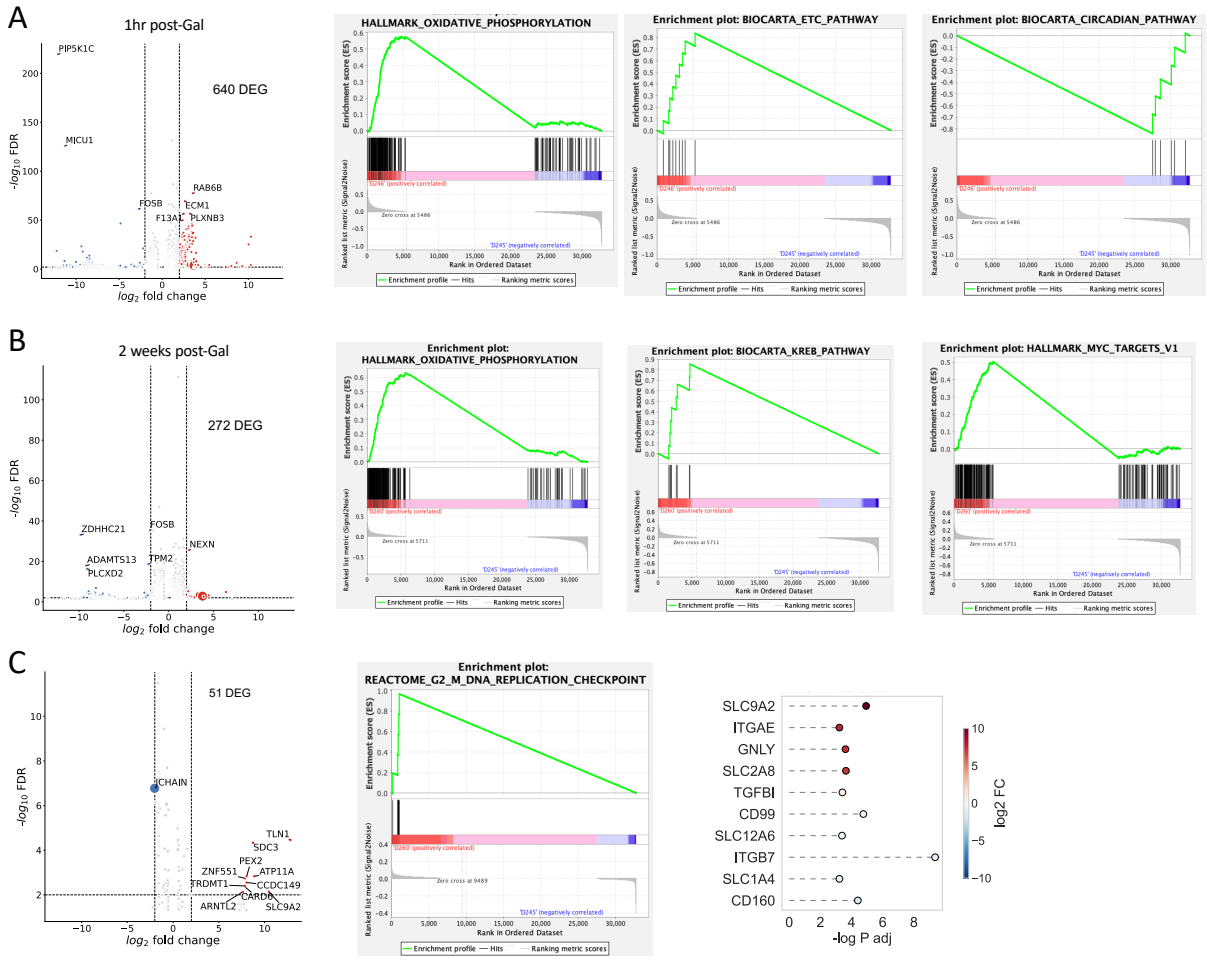

Figure 5. OXPHOS and other metabolic pathways increase rapidly with TGF-β blockade. A-C) Bulk RNAseq was performed with PBMC from before cycle 1 (24hrs) and 1hrs after the first dose of galunisertib (A) or after the last dose of cycle 1 (B) and with rectal biopsies collected before cycle 1 (24hrs) and after the last dose of cycle 1 (C). The number of differentially expressed genes (DEG) with an FDR <0.05 and abs(log_2FC)>2 are shown in each respective volcano plot. Enrichment plots are shown after GSEA (with all FDR<0.05 DEGs) for significantly enriched pathways (top 1 or 2 pathway by ES). C) Lollipop graph of selected DEG of interest among significantly different genes (FDR<0.05).

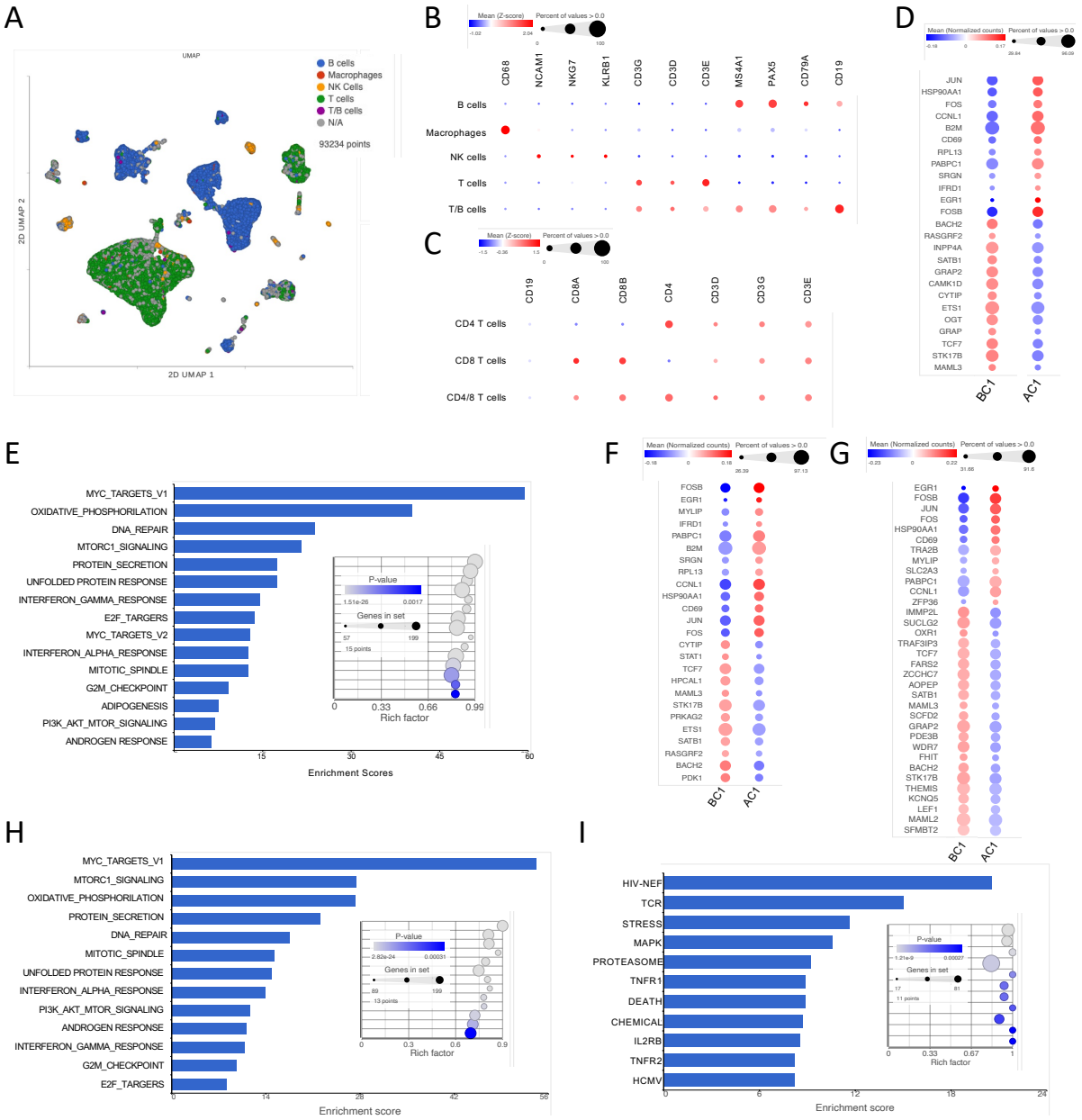

980 **Figure 6. scRNAseq of lymph node before and after cycle 1 confirms a switch toward**
981 **effector and increased metabolism in all immune subsets with galunisertib.** A) UMAP
982 projection of 93234 cells from lymph nodes collected right before and at the end of cycle 1 from
983 all 8 macaques (16 samples). Gene-based classification of major immune subset is overlaid on
984 UMAP. In gray are unclassified cells. B-C) Bubble plots showing expression (mean normalized
985 counts proportional to the color; size proportional to the percentage of cells) of each marker listed

986 in each cell subset. Marker listed are those used for classification of major immune subsets (B)
987 or CD4$^+$ and CD8$^+$ T cells (C). D) Significantly different genes (FDR<0.05; log2FC=0.15) in the T
988 cell subset are shown with color proportional to normalized counts. E) Significantly enriched
989 pathways (FDR<0.01) in T cells DEGs within the hallmark collection. F-G) Significantly different
990 genes (FDR<0.05; log2FC=0.15) in the CD4$^+$ (F) and CD8$^+$ (G) T cell subset. H-I) Significantly
991 enriched pathways (FDR<0.01) in CD4$^+$ T cells DEGs within the hallmark (H) and biocarta (I)
992 collections.
993

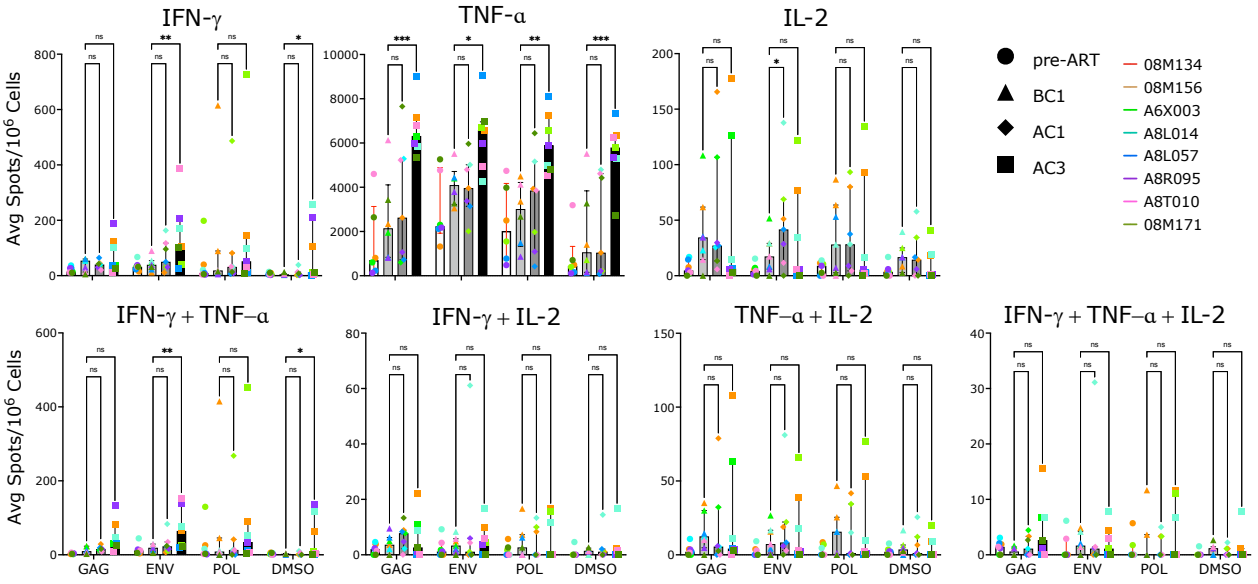

994 **Figure 7. Galunisertib increases SIV-specific responses.** Average spots (from triplicates) per
995 10^6 PBMC at the time of ART initiation (pre-ART), before cycle 1 (BC1), after cycle 1 (AC1) and
996 at the end of cycle 3 (AC3) with galunisertib after 24hrs ex vivo stimulation with 15-mer peptides
997 (gag, env, pol) or mock (DMSO). Each post-galunisertib time point was compared to BC1 (Mixed
998 effect analysis with Dunnet post-hoc p-values are shown; *p≤0.05 **p≤0.01 ***p≤0.001)

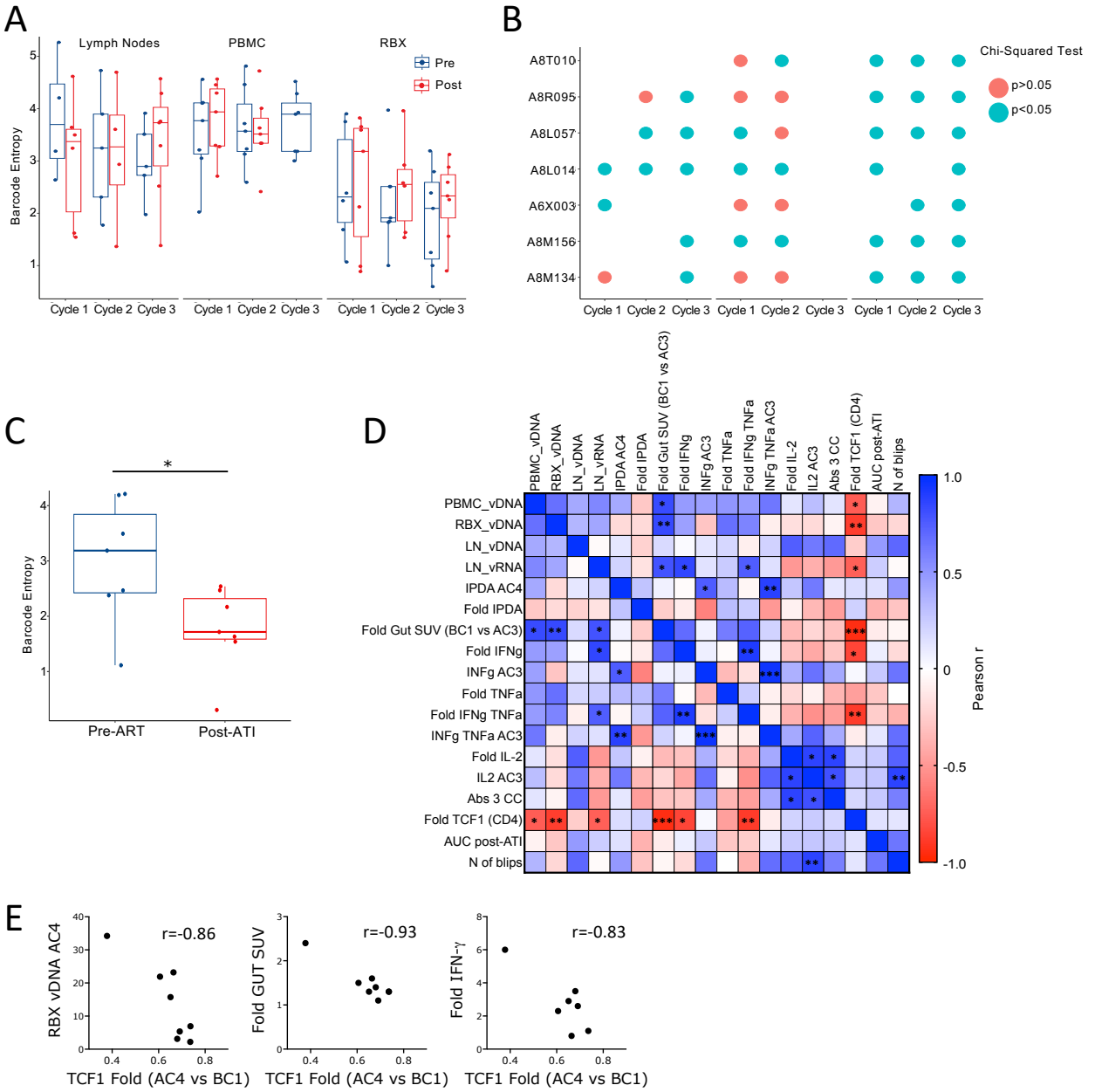

Figure 8. TCF1 decrease associates with virological and immunological endpoints. A) Barcode diversity measure as Shannon Entropy is shown before and after each of the first 3 galunisertib cycles for LN, PBMC and colorectal biopsies. Box-and-whisker plot represents the median +/− the interquartile range (no significant differences using linear mixed effects models). Blue= before; Red= end of each cycle. B) Bubble plot shows the results of statistical testing (Chi-squared) for differences in frequency distribution of barcodes before compared to after, for each

1006 of the first 3 cycles of galunisertib for each macaque in the indicated tissues. Blue indicates
1007 significant differences $p \leq 0.05$. C) Barcode entropy of virus isolated at the time of ART initiation
1008 compared to week 6 post-ATI in plasma (Wilcoxon matched pairs test; $*p \leq 0.05$). D) Correlation
1009 matrix of several key variables of virological or immunological effect of galunisertib. Color is
1010 proportional to Pearson r coefficient. $*p \leq 0.05$ $**p \leq 0.01$ $***p \leq 0.001$ indicate significant correlations.
1011 F) Association between fold increase in TCF1 (MFI) from BC1 to AC4 with CA-vDNA levels at
1012 AC4, change in gut SUV at AC3 compared to BC1 and fold increase in IFN-γ (AC3 vs BC1).
1013 Person r is shown. All correlations have $*p \leq 0.05$.

1014
1015
1016